Journal of Building Engineering 113 (2025) 113991

Contents lists available at ScienceDirect

Journal of Building Engineering

journal homepage: www.elsevier.com/locate/jobe

Full length article

Overstrength and variance analysis of angle brackets for timber structures considering the uncertainty in the nail–timber interaction

Petr Sejkot [a], Angelo Aloisio [b,*], Yuri De Santis [b], Massimo Fragiacomo [b], Asif Iqbal [c]

[a] Klokner Institute, Czech Technical University in Prague, Šolínova 7, 166 08 Praha 6 – Dejvice, Czech Republic
[b] Department of Civil, Construction-Architectural and Environmental Engineering, Università degli Studi dell'Aquila, L'Aquila, 67100, Italy
[c] University of Northern British Columbia, 3333 University Way, Prince George, BC V2N 4Z9, Canada

ARTICLE INFO

Keywords:
Angle brackets
Overstrength factor
FE modelling
Uncertainty quantification
Monte Carlo analysis

ABSTRACT

Engineered wood products, along with advanced processing and fabrication, are pushing the limits of modern wood construction. However, the capacities of such systems are often determined by the capabilities of the connections. Typical connections for timber beams consist of angle brackets with annular ring nails. The load-bearing capacity of these connections is usually provided by their producers and is based on experimental testing, where the connection is typically subjected to short-term monotonic loading. However, the variability of angle bracket capacity is generally governed by uncertainties on the timber side, specifically the interaction between nails and wood. This paper presents the experimental results and a parametric numerical element model for predicting the load-bearing capacity of connections with nailed angle brackets, considering the effects of uncertainties in the nail–timber constitutive behaviour. Three metal brackets for beam–column connections are analysed, and their performance in various loading arrangements is examined. Detailed finite element models have been developed for each connection, where the response of each nail is defined by a semi-physical constitutive relationship calibrated on separate axial and transversal tests on isolated nails. The authors propagate the uncertainty in the nail–timber interaction on the capacity of the angle brackets following a Monte Carlo-based approach in the three considered loading scenarios. The generated dataset is used to estimate the overstrength factors of the connections and explain the variance of the estimated capacity values based on a multilinear regression surrogate model.

1. Introduction

The growth in the use of wooden structures has been marked by the advent and spread of cross-laminated timber (CLT). CLT is an engineered wood product notable for its optimal structural and thermal performance [1–3]. These attributes make CLT an advantageous building material for floor diaphragms or shear walls in medium and high-rise timber structures.

If the authors were to draw an ideal timeline for the last 20 years, the more substantial studies of wooden structures initially focused on the CLT wall panel. Then, they shifted to the interaction between CLT panels and connectors. Wooden buildings are predominantly assembled using dry joints with steel connectors. CLT wall panels are typically connected to foundations or floor diaphragms using hold-downs and angle brackets, creating a characteristic CLT shear wall structure. These hold-downs and angle

* Corresponding author.
E-mail addresses: petr.sejkot@cvut.cz (P. Sejkot), angelo.aloisio1@univaq.it (A. Aloisio), yuri.desantis@univaq.it (Y. De Santis), massimo.fragiacomo@univaq.it (M. Fragiacomo), asif.iqbal@unbc.ca (A. Iqbal).

https://doi.org/10.1016/j.jobe.2025.113991
Received 20 June 2024; Received in revised form 28 August 2025; Accepted 1 September 2025
Available online 20 September 2025

brackets are usually fastened to the floor diaphragms with screws or nails or anchored to the foundation using bolts. The CLT wall panels' high in-plane strength and stiffness enable them to behave rigidly with an elastic response. Therefore, the mechanical properties of the hold-downs or angle brackets largely determine the seismic performance of the CLT shear wall structures [4–6].

Over the past 15 years, numerous studies have demonstrated the capabilities and nature of connections in CLT with hold-downs and angle brackets [7]. Investigations into CLT primarily began with examining the mechanical properties of standard connections, such as hold-downs and angle brackets, laying the groundwork for further exploration of CLT shear walls. Gavric et al. [8] performed hysteretic tests on these connections, applying cyclic loads in both vertical and horizontal directions and discovering notable ductility and energy dissipation. Tomasi and Smith [9] examined wall-to-foundation angle brackets, underscoring the importance of experimental studies in determining connection capacities. Hossain et al. [9] explored using self-tapping screws with a double inclination in CLT panel connections, revealing improved structural performance and necessary ductility. Izzi et al. [10] carried out vertical tension tests on steel-to-timber joints, finding agreement between experimental capacities and those predicted by European Technical Assessment [11]. Sun et al. [12] analysed seismic behaviours of CLT shear walls with U-shaped flexural plate connections, confirming their effectiveness in reducing seismic-induced horizontal accelerations.

Most studies treat the rocking and slip mechanisms of shear walls as independent. However, in multi-story CLT shear wall structures under seismic loads, these mechanisms jointly affect the wall-to-floor and wall-to-foundation connections. Liu and Lam [13,14] investigated the tension-shear coupling effect in CLT connections, finding axial tension to significantly influence shear resistance. Liu et al. [15] modelled this coupling effect using the HYST algorithm. Pozza et al. [16] tested the tension-shear coupling in wall-to-foundation hold-downs, noting the influence of lateral deformation on axial properties. They later developed a numerical model [17] for predicting the coupled tension-shear response under various loading scenarios. Masroor et al. [18] studied the bi-axial influence of angle brackets on CLT shear walls, noting the significance of considering the coupling effect in engineering design. Sun et al. [19], and Sejkot et al. [20] further emphasize this point, focusing on the hysteretic response of ductile connections with nailed angle brackets in mass timber structures.

So far, it has become manifest that steel connections for CLT possess high capacity and dissipation [21–23]. This ductility generally originates from fastener and timber plasticization [24,25]. However, they also exhibit significant degradation in strength and ductility after repeated cycles, resulting in reduced structural robustness [26,27]. From this conclusion, drawn from multiple experimental campaigns, especially on shaking tables [28,29], various research aspects have emerged seeking to improve the dissipative capacity of connections for wooden buildings, mitigate their strength degradation, develop pinching-free connections [30], or conceive new construction systems without strength degradation, termed resilient, like post-tensioned rocking walls [31,32].

However, these attempts to improve connection systems in wooden buildings, particularly in CLT, have remained niche products except in a few cases, like friction hold-downs, which have found a market presence [33]. Most CLT buildings still rely on off-the-shelf brackets (hold-downs, shear keys) initially developed for LTF buildings [21,34,35]. While it is important to direct research efforts towards new construction solutions, it is equally important to continue studying traditional connections, as they are the most widespread. Moreover, while much research has been devoted to experimentation, less attention has been given to refined modelling of these systems [36–39] and even less to understand the reasons and causes of the uncertainty associated with estimating the capacity of the connections.

This uncertainty in capacity is significant as it is related to the concept of the hierarchy of resistances [40–42], a guiding principle of seismic design condensed into a factor known as overstrength [43]. In other words, underestimating capacity can lead to non-conservative design, which is dangerous.

Therefore, characterizing the uncertainty of the capacity of CLT connections is crucial for safe design at the connection [7,21,22,44–48] and system levels [21,29,49–51]. Typically, uncertainty is characterized based on experimental data, yet as shown, the limited number of repetitions and laboratory conditions are often associated with less uncertainty than what would realistically occur [43,52]. Thus, it is important to characterize uncertainty by considering material uncertainties and the interaction between steel and wood to obtain a realistic picture of capacity scatter [53].

This study presents the case of steel angle brackets used for CLT connections. The main novelty of the work is the characterization of the uncertainty of the bracket's capacity by propagating the uncertainty of the nail-wood relationship. This aims to propose a conscious estimate of the overstrength and to understand the main sources of uncertainty.

After a preliminary characterization campaign, necessary for the authors to have access and full control for appropriate modelling, a high-fidelity model of the angle bracket with screws was developed. Assuming the timber-screw constitutive law with its associated uncertainty from the literature and adopting an innovative parametrization based on [54], the model was first validated and then used to characterize the uncertainty of the angle bracket's response under three loading directions: extraction, shear, and rocking (horizontal load with offset). The study then estimated overstrength factors according to two formulations in [43,55], providing a relative estimate of the uncertainty of the capacity of the angle brackets. The generated dataset was then used to calibrate a surrogate model to explain the total variance of the output and understand the main sources of uncertainty in the capacity of angle brackets. As a final step, the results from Monte Carlo analysis led to the overstrength factor assessment, which was compared against the estimations from the existing literature

This work advances research on CLT connection systems by moving beyond point-capacity or purely experimental characterizations and, instead, quantifying and explaining the variability and overstrength of widely used nailed angle brackets under uplift, shear, and rocking. The contribution is fourfold: (i) the authors stochastically propagate fastener–timber uncertainties — identified from isolated axial and transverse nail tests — through a validated, high-fidelity yet computationally efficient FE model of the bracketed connection; (ii) they adapt and parameterize an empirical withdrawal/lateral constitutive law for nails to enable Monte Carlo sampling and connection-level response distributions; (iii) they introduce an interpretable surrogate-regression framework that

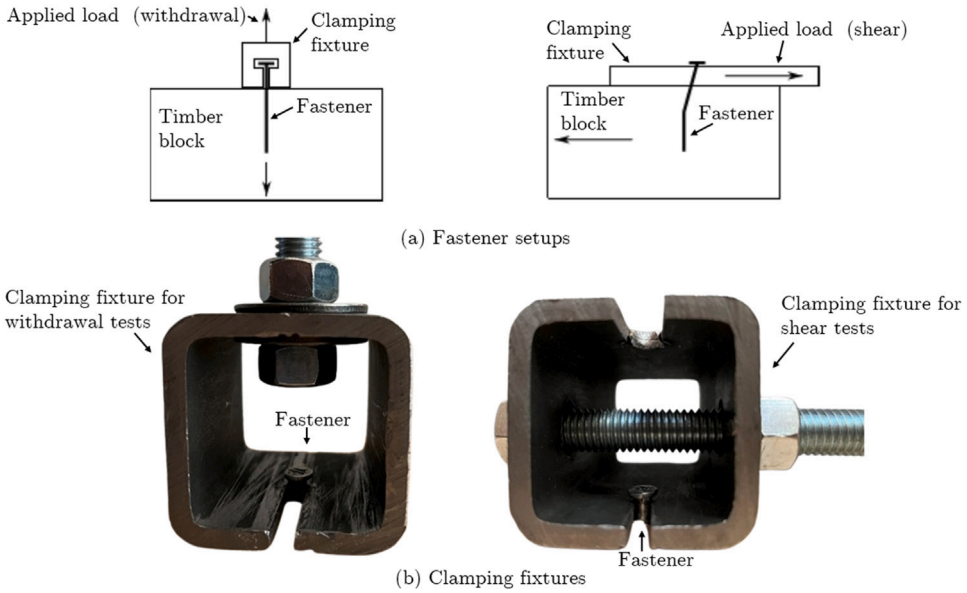

Fig. 1. (a) Single-fastener test schematics: withdrawal (left) and lateral shear (right). (b) Custom fixtures used in the tests.

apportions capacity variance to physical inputs, clarifying that withdrawal strength governs uplift/rocking while lateral resistance controls shear (with typical CoV ≈ 18% for uplift, 13% for rocking, and 4%–5% for shear); and (iv) they translate these distributions into reliability-consistent overstrength factors using both the Jorissen–Fragiacomo formulation and a model-driven formulation with explicit target reliability. This procedure yields code-aligned guidance for capacity design and hierarchy-of-resistance checks in CLT structures, providing an advancement over prior deterministic or connector-specific studies.

2. Experimental tests

To characterize the uncertainty in the capacity of the angle brackets, the authors conducted two experimental tests. The first series focused on the single fastener, testing the nail in axial and transversal directions to calibrate a representative constitutive relationship. The second series evaluated a structural subassembly consisting of angle brackets and timber elements under three loading directions.

2.1. Fasteners tests

Fig. 1 shows the test setup used to independently test the nails in axial and transversal directions. The obtained force–displacement curves are then used to characterize an equivalent constitutive relationship of the nail in both directions.

No international standard specifies a monotonic procedure to isolate the constitutive law of a single annular-ring nail in CLT under either pure withdrawal or pure lateral action with the boundary conditions required for model calibration. For this reason, a purpose-built steel fixture was designed (Fig. 1), able to (i) align the applied load with the nail axis for withdrawal and with the grain-perpendicular direction for lateral loading, and (ii) prevent eccentricities and block rotation of the timber block, so that the measured response corresponds to the nail–timber relative slip used in the modelling. Tests were conducted under displacement control on a universal testing machine, using a 10 kN class load cell for this series; force and slip were recorded from the machine, and an LVDT tracked the relative movement between the nail head and timber surface.

The tested nails are CNA4.0X60, produced by Simpson Strong-Tie, with a length of 60 mm and a diameter of 4 mm [56]. CNA nails are annular ring shank connector nails with a conical shape under the head. They are inserted into a CLT element with 3 layers, a thickness of 99 mm and average mass and moisture content of 481 kg/m^3 and 12%, respectively. A total of 3 shear tests and 10 pull-out tests were conducted.

Tables 1 and 2 show the experimental results of the shear and pull-out tests, respectively. They report the initial stiffness (k_i), slip modulus (k_s), ultimate force (f_u), ultimate displacement (u_u), residual stiffness (k_r), and residual capacity (f_r) of the nail. As expected, transversal test results are characterized by less dispersed values than axial test results.

Fig. 2 shows the force–displacement curves for the two groups of tests in the axial and transversal directions.

To characterize the force–displacement relationship of the single nail in withdrawal using a semi-empirical approach for the parametric FE model of the angle bracket, the authors adopted an empirical constitutive relationship initially developed for screw

Table 1
Initial stiffness (k_i), slip modulus (k_s), ultimate force (f_u), ultimate displacement (u_u), residual stiffness (k_r) and residual capacity (f_r) of nail in transversal loading.

Configuration	k_i (kN/mm)	k_s (kN/mm)	f_u (kN)	u_u (mm)	k_r (kN/mm)	f_r (kN)
T-1	0,28	0,24	4,46	17,17	0,04	1,20
T-2	0,28	0,25	4,48	16,83	0,09	1,38
T-3	0,28	0,24	5,06	18,92	0,09	1,32
Avg.	**0,28**	**0,25**	**4,67**	**17,64**	**0,07**	**1,30**
CoV	<1%	2%	6%	5%	28%	6%

Table 2
Initial stiffness (k_i), slip modulus (k_s), ultimate force (f_u), ultimate displacement (u_u), residual stiffness (k_r) and residual capacity (f_r) of nail in axial loading.

Configuration	k_i (kN/mm)	k_s (kN/mm)	f_u (kN)	u_u (mm)	k_r (kN/mm)	f_r (kN)
W-1	1,47	1,68	2,45	3,08	0,06	0,38
W-2	3,91	3,70	2,80	2,28	0,05	0,98
W-3	1,21	1,08	3,14	3,62	0,10	0,55
W-4	0,82	0,78	2,12	2,83	0,05	0,32
W-5	1,84	1,69	2,75	3,15	0,07	0,65
W-6	1,19	1,01	1,82	2,40	0,05	−0,02
W-7	1,29	1,04	1,88	2,30	0,01	−0,12
W-8	2,06	1,91	2,04	1,95	0,05	0,21
W-9	1,01	1,40	2,60	2,67	0,05	0,27
W-10	1,54	2,37	2,28	1,95	0,05	0,44
Avg.	**1,63**	**1,67**	**2,39**	**2,62**	**0,05**	**0,37**
CoV	51%	49%	17%	20%	43%	83%

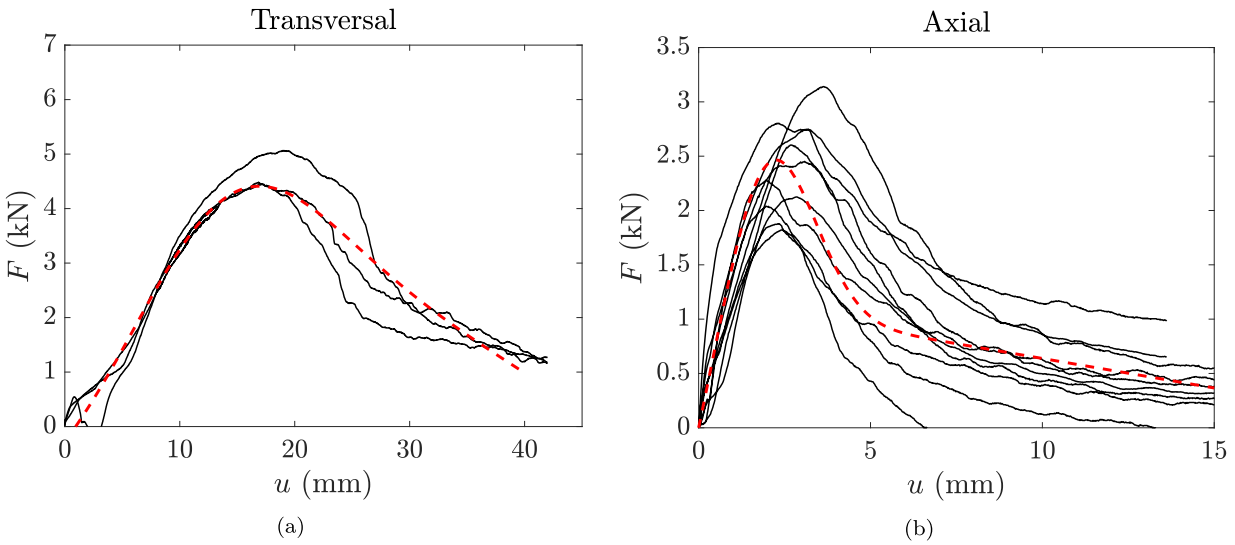

Fig. 2. Experimental (black) and calibrated constitutive model (red dashed) force–displacement curves for fastener in (a) transversal loading, (b) axial loading.

withdrawal in [57]. To the author's knowledge, no specific empirical models have been developed for nails in withdrawal. The model described by Eq. (1) proved to be adequate for also describing the behaviour of the nails (Fig. 2(b)).

$$f(u) = c\left[1 + 4e^{-\frac{u^{5/2}}{r}} \sin\left(\frac{u-t}{r} l\pi\right)\right] - d \cdot u \tag{1}$$

Where $f(u)$ is the reaction force on the fastener, and u represents the axial or transversal displacement. The parameters c, d, t, l are empirical parameters that relate to the corresponding physical parameters f_u, f_r, u_u, k_r, which represent ultimate capacity, residual capacity, ultimate displacement, and secant stiffness, respectively. Specifically, in Eq. (1) d equals the residual secant stiffness between 7.5 mm and 15 mm slip (or residual stiffness k_r), and f_r is the residual strength at 15 mm. The other mechanical

Table 3
Empirical model parameters defined in Eq. (1) for the transverse (T) and axial (W) directions.

Configuration	c	CoV	t	CoV	l	CoV	d	CoV	r	CoV
T	6,32	13%	1084,65	19%	7,28	15%	0,13	15%	1298,51	4%
W	1,18	49%	0,74	39%	1,63	87%	0,05	43%	15,00	0%

parameters are the conventional parameters, namely the strength f_u and the ultimate displacement u_u. The fictitious parameters in Eq. (1) can be calculated from the mechanical parameters through the following equations:

$$d = k_r \tag{2}$$

$$c = 15k_r + f_r \tag{3}$$

$$t = \frac{u_u \arcsin\left(\frac{1}{4}\right)}{\arcsin\left(\frac{1}{4}\right) + \arcsin\left(\frac{e^{-\frac{u_u^{5/2}}{15}}(-15k_r + f_u - f_r + k_r u_u)}{4(15k_r + f_r)}\right)} \tag{4}$$

$$l = \frac{15}{\pi t}\arcsin\left(\frac{1}{4}\right) \tag{5}$$

The same empirical model has been used to describe nail transversal behaviour. It is worth mentioning that several empirical models for describing the transversal behaviour of metal fasteners exist, e.g. Foschi [58] and Richard-Abbott [59] empirical models. However, these models are not able to describe the post-peak softening. Using Eq. (1) for the transversal behaviour required a re-definition of k_r and f_r. In this case, the residual stiffness is the secant stiffness between 30 mm and 40 mm slip, and f_r is the residual strength at 40 mm.

The mean curve associated with Eq. (1) is shown in dashed red in Fig. 2. The authors calibrated the parameters in Eq. (1) for each experimental curve, estimating the corresponding coefficients of variation for uncertainty propagation in subsequent steps.

Table 3 reports the mean parameters of the proposed model and the corresponding coefficients of variation for both the transversal (T) and axial (W) directions.

2.2. Connection tests

Monotonic tests were performed on CLT connections with brackets in three loading arrangements. Three types of brackets, all made by Simpson Strong-Tie: HGA10, ABR9020, and ABR105 (Simpson Strong-Tie 2019), were used for each setup and shown in Fig. 3.

The monotonic tests on CLT connections with angle brackets (HGA10, ABR9020, ABR105) were performed in accordance with EN 12512 for joints with mechanical fasteners. Each specimen comprised three CLT blocks with two brackets. The tests were carried out with a Universal Testing Machine at the Wood Innovation Research Laboratory of the University of Northern British Columbia. Tests were run under displacement control at a quasi-static rate until a clear post-peak response, measuring displacement at the actuator. For rocking, the horizontal force was applied 205 mm above the shear plane.

In all arrangements, the two outer CLT blocks were anchored to the laboratory strong floor using steel clamping beams and through-bolts. Horizontal restraint was provided by the clamp normal force (base friction) and by screwed timber cleats with a toothed profile bearing on the block sides to prevent in-plane rotation. The intermediate CLT block was not clamped and interacted with the supports only through the two angle brackets. A 3 mm gap was maintained between adjacent blocks to eliminate bearing and friction between the blocks themselves. The actuator load was applied at the points indicated by the red dot in Fig. 4: vertical for uplift, horizontal in the shear plane for sliding, and horizontal at an eccentricity of 205 mm above the shear plane for rocking.

HGA10 is a “Hurricane Gusset Angle” made of 1.86 mm thick (14 gauge) galvanized steel sheet. Its dimensions are 88.9 mm (3.5 in.) in width, 76.2 mm (3 in.) in height, and 50.8 mm (2 in.) in depth. ABR9020 and ABR105 are “Angle Brackets for Cross-Laminated Timber”. ABR9020 is a 2.0 mm thick (14 gauge) galvanized steel sheet. Its dimensions are 65.1 mm (2.5625 in.) in depth and 87.3 mm (3.4375 in.) in width and height. ABR105 is made of 3.0 mm thick (11 gauge) galvanized steel sheet. Its dimensions are 90.5 mm (3.5625 in.) in depth and 104.8 mm (4.125 in.) in width and height. ABR9020 and ABR105 brackets can be produced from any stainless steel with a minimum characteristic 0.2% yield stress of 240 MPa, a minimum 1.0% yield stress of 270 MPa, and a minimum ultimate tensile strength of 530 MPa. In this particular case, angle brackets made of S250GD+Z275 were used. HGA10 brackets are manufactured from galvanized steel complying with ASTM A653, Grade 33, SS designation with a minimum yield strength of 33,000 psi (227 MPa) and a minimum ultimate tensile strength of 45,000 psi (310 MPa). The connectors have a minimum G90 zinc coating designation complying with ASTM A653. Wood members with which the connectors are used can be either sawn or engineered timber.

Table 4 displays the test matrix with all configurations. Each of the three angle brackets is tested in three directions, designated as uplift (U), shear (S), and rocking (R). The rocking tests involve applying a lateral force at the height of 205 mm from the base of the angle bracket to generate bending moment on the bracket.

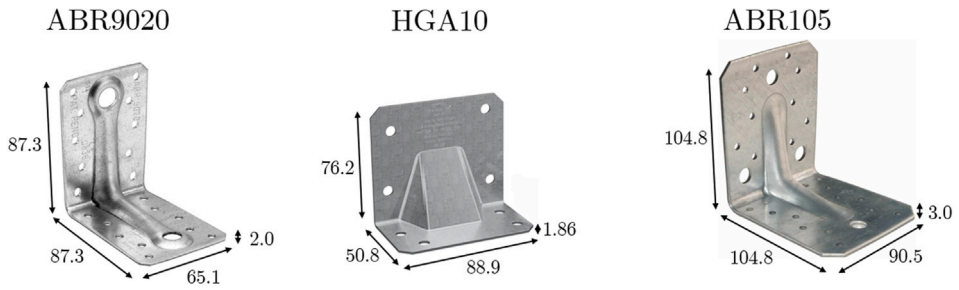

Fig. 3. Picture and main characteristics of the tested angle brackets. All dimensions are expressed in mm.

Table 4
Tested configurations where l_p and d are the penetration depth and diameter of the nail.

Label	Loading	Fastener type	Fastener number (n°)	l_p (mm)	d (mm)
ABR9020-U	Uplifting	CNA nails	2 × 20	60	4
HGA10-U	Uplifting	CNA nails	2 × 4	60	4
ABR105-U	Uplifting	CNA nails	2 × 24	60	4
ABR9020-R	Rocking	CNA nails	2 × 20	60	4
HGA10-R	Rocking	CNA nails	2 × 4	60	4
ABR105-R	Rocking	CNA nails	2 × 24	60	4
ABR9020-S	Sliding	CNA nails	2 × 20	60	4
HGA10-S	Sliding	CNA nails	2 × 4	60	4
ABR105-S	Sliding	CNA nails	2 × 24	60	4

No external LVDTs were mounted on the CLT blocks. The displacement u used in the load–displacement curves corresponds to the testing machine actuator stroke measured at the same point where the force F was applied. Accordingly, in Fig. 4, the red dot and arrow mark both the load application and the displacement reading. Fig. 5 displays the photographic views of the connection test setups.

Fig. 4 displays each arrangement's technical drawings, including the brackets' shape and position.

All the test setups consisted of three CLT blocks and two angle brackets. Two CLT blocks were secured to the floor, and one CLT block was placed between them, each connected to a fixed block by an angle bracket. A 3 mm gap was maintained between the blocks to prevent friction between the CLT members. In the rocking test setup, the load was applied at the top of the intermediate CLT panel, 205 mm from the shear plane. In the shear test setup, the load was applied at the top of the intermediate CLT panel, directly in the shear plane of the connection. In the pull-out test setup, the load was applied at the top of the intermediate CLT block, aligning with the centre of the connection.

Fig. 6 displays the experimental curves for the nine test configurations involving three loading directions for the three angle brackets. The experimental results show that, on average, the strongest direction in all three angles is lateral. In some cases, the lateral capacity is comparable to uplift, although occasionally slightly lower, as detailed in Table 5. The lowest capacity values are associated with the rocking curves, which are only about 1/4 to 1/5 of those for shear or extraction. ABR105 has the highest capacity, followed by ABR9020 and HGA10. The HGA is the smallest and most compact shape, resulting in relatively low capacity. The sharp drop in load indicates the pullout of the nails. In contrast, the other two brackets allow significant deformation after the metal yields while resisting the load before the eventual pullout of the nails. Interestingly, the uplift behaviour is markedly ductile, as does rocking, while the shear response is highly brittle. Once the capacity value reaches about 20 mm, resistance is sharply degraded. Therefore, the connection exhibits ductile behaviour when subjected to axial forces or torque and brittle behaviour when subjected to shear forces.

Fig. 7 shows the failure modes corresponding to the nine experimental tests. Regarding the pull-out tests, the first two rows of nails were completely extracted in all angle brackets. Specifically, in the HGA105 test, nearly all nails in two rows were extracted from one wing of the angle bracket.

As previously noted, the nails did not reach their shear resistance; instead, failure occurred on the timber side with incipient splitting caused by the short distance between the end of the angle bracket and the wood element's edges, approximately equal to 51.5 mm (ABR9020), 41.0 mm (ABR105) and 39.5 mm (HGA10). In the rocking tests, the failure modes predominantly showed pull-out with slight transverse deformation of the first two rows of nails. Significant deformation was observed for the ABR9020 angle bracket, especially in pull-out and rocking tests. Lesser deformation was seen in the ABR105 due to more nails and larger dimensions of the angle bracket. Regarding the HGA angle bracket, deformation was concentrated around the rib, which showed no signs of deformation due to its larger size than the ABR series.

Table 5 summarizes the main parameters of the experimental curves: initial stiffness (k_i), slip modulus (k_s), ultimate force (f_u) and ultimate displacement (u_u) of connections. The initial slip modulus measures the stiffness of the connection in the first loading

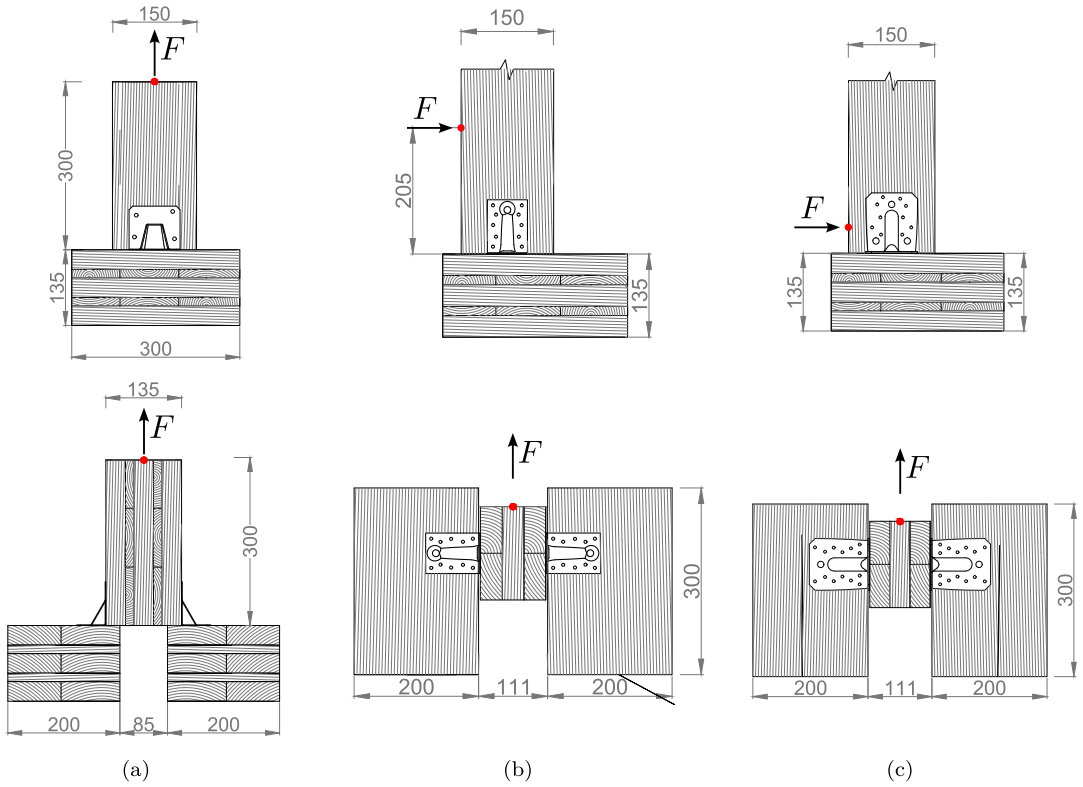

Fig. 4. Connection test setup schemes: (a) uplifting, (b) rocking, and (c) sliding. The red dot and arrow indicate the application point and direction of the load F and the location/direction of the displacement measurement u (machine actuator stroke). Dimensions in mm.

Table 5
Connection experimental parameters: initial stiffness (k_i), slip modulus (k_s), ultimate force (f_u) and ultimate displacement (u_u) of connections.

Configuration	k_i (kN/mm)	k_s (kN/mm)	f_u (kN)	u_u (mm)
ABR9020-U	3,73	3,68	18,2	7,9
ABR9020-R	0,06	0,06	3,5	79,7
ABR9020-S	2,37	2,48	32,2	24,1
HGA10-U	0,22	0,30	13,5	14,5
HGA10-R	0,14	0,14	2,7	53,1
HGA10-S	1,21	1,29	19,7	18,0
ABR105-U	3,71	0,27	36,0	9,6
ABR105-R	0,20	0,18	7,8	82,3
ABR105-S	2,23	2,25	33,0	21,4

phase, and it is determined with the following definition:

$$k_i = \frac{0.4F_{max}}{v_{04}} \tag{6}$$

where F_{max} is the maximum load and v_{04} is the connection displacement at $0.4F_{max}$.

Following EN 12512 [60], the slip modulus is evaluated as the secant stiffness between $0.1F_{\max}$ and $0.4F_{\max}$ in the first loading phase:

$$k_s = \frac{0.4F_{\max} - 0.1F_{\max}}{v_{04} - v_{01}}, \tag{7}$$

where v_{04} and v_{01} are the relative slips corresponding to $0.4F_{\max}$ and $0.1F_{\max}$, respectively (see also EN 26891 [61]).

It is observed that the most rigid directions for ABR9020 and ABR105 are the axial ones, followed by shear and then rocking. The HGA10 geometry makes it more rigid in shear, followed by the axial direction and rocking. The secant stiffness values are equivalent

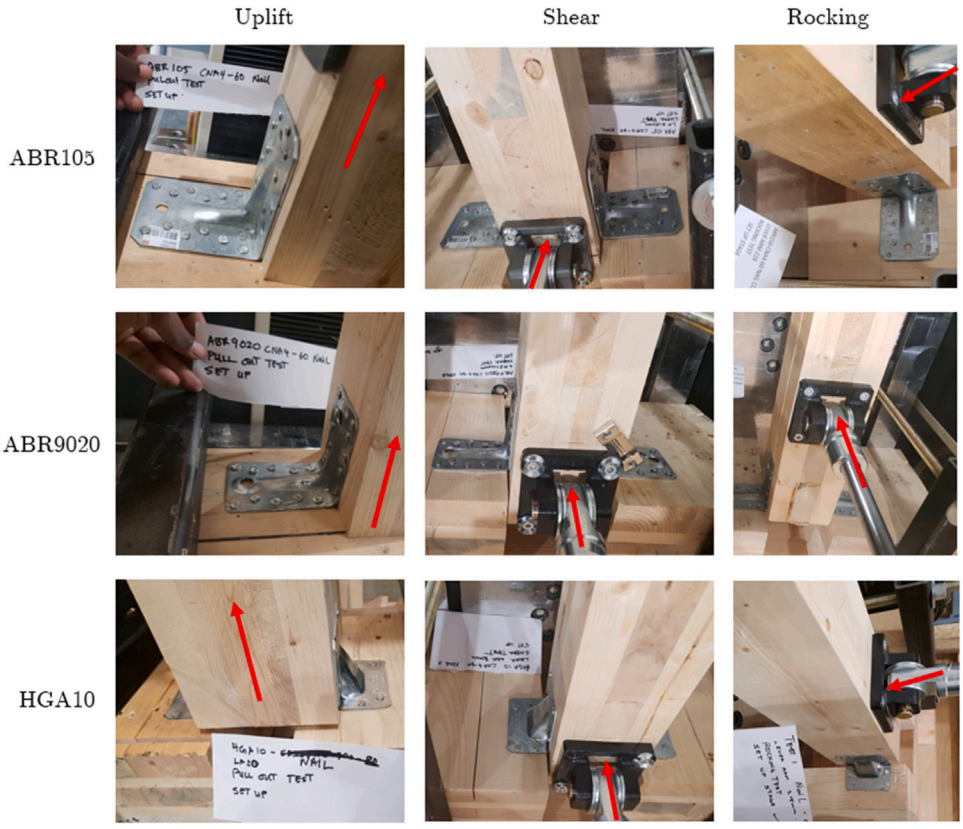

Fig. 5. Photographic views of the connection test setups. Columns: Uplift, Shear, Rocking. Rows: ABR105, ABR9020, HGA10. Red arrows indicate the load direction.

to the initial values overall. The capacity values, already discussed in the previous paragraph, confirm significant resistance in the axial and transverse directions, which are comparable.

It should be noted that, in this study, the dispersion of connection capacity is not inferred from repeated connection tests. Instead, the authors identify the uncertainty of the nail–timber constitutive laws from single-fastener tests (withdrawal and lateral) and propagate these distributions through the validated FE model by Monte Carlo simulation to obtain capacity distributions for each bracket and loading scenario. This design separates model validation (full-scale tests) from uncertainty identification (fastener tests), enabling broad exploration of variability without an impractically large number of full-scale replicates.

3. Numerical model of the connection

The authors developed a parametric model of the nine experimental tests obtained by considering three angle brackets under the three load configurations. The model, developed in Abaqus, represents a trade-off between complexity and accuracy. As shown in Fig. 8, the geometry of the CLT elements and the angle bracket are represented in their actual three-dimensional shape and size. However, the nails are modelled as equivalent springs in the transverse and axial directions, with relationships defined in Eq. (1). The parametrization in the model lies in the possibility of semi-automatically run analyses on the angle bracket by assigning, for each simulation, randomly generated force–displacement curves for spring representing the timber–nail interaction, as will be clarified in the following section.

To enable the Monte Carlo campaign at reasonable cost, the model uses a mixed discretization. Only one half of the connection (one bracket) is analysed, assuming load sharing between the two brackets by symmetry. The remote parts of the CLT members that do not come into contact with the bracket are modelled with Euler–Bernoulli beam elements to reproduce the global stiffness. The near-bracket timber region is modelled with laminated orthotropic shell elements (ply lay-up [0/90/0] consistent with the 3-ply CLT, total thickness 135 mm), while the steel brackets are also discretized with general-purpose shell elements. In the implementation the authors used 3-node triangular shells (S3, finite-membrane-strain) with a nominal in-plane seed of 2 mm; a mesh-refinement study (halved element size) changed capacity by <5%. The apparent "solid" appearance in Figs. 5 and 9 is due to the postprocessor rendering the assigned shell thickness. Contact between the bracket and timber shells is frictionless in the tangential direction and hard in the normal direction. Nails are not meshed as solids: each nail is represented by a 2-node connector (wire/spring) that links a node on the bracket shell to the corresponding node on the timber shell. The connector has two orthogonal nonlinear degrees of

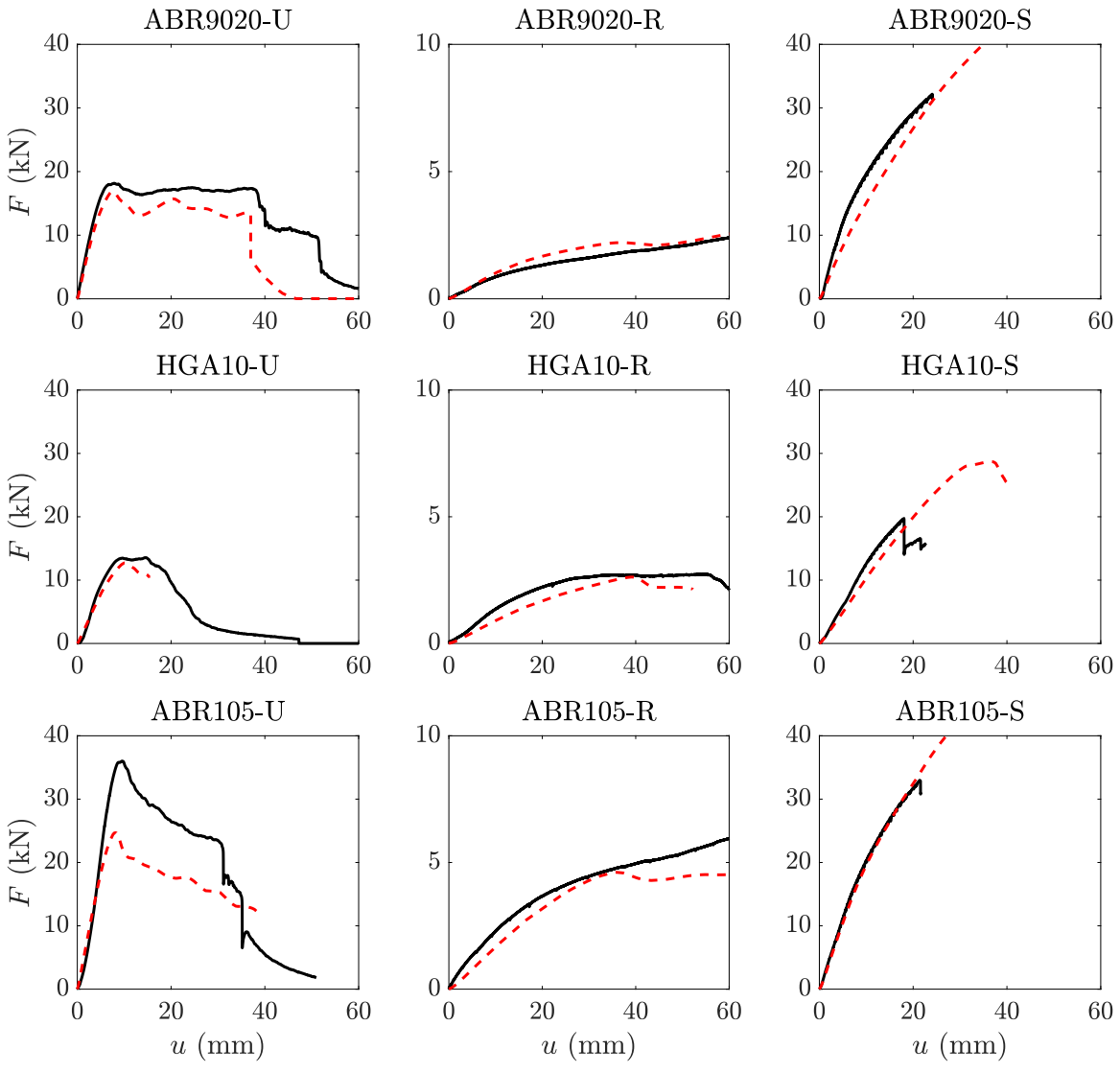

Fig. 6. Force–displacement experimental curves (solid line); Numerical predictions (dashed curves).

freedom: (i) axial along the nail (withdrawal) and (ii) in-plane transverse slip, each governed by the empirically calibrated laws in Eq. (1) with parameters in Table 3. This formulation allows shell-type timber and bracket meshes to be coupled consistently to the fastener mechanics without resorting to volumetric meshing of the wood.

The outer blocks, anchored as described above, were idealized as clamped supports in the FE model (translations and rotations restrained at the anchorage lines), consistent with the clamped-and-cleated test boundary condition.

The experimentally obtained load-to-displacement data for the nails describe only the displacement of the nail head relative to the centreline of the timber beam, meaning the Abaqus model does not simulate the deformation of the wire's steel shank or the degradation of the surrounding timber material.

The timber material was defined using nine engineering constants (E_l = 9700 MPa, E_r = 400 MPa, E_t = 220 MPa, ν_{lr} = 0.3, ν_{lt} = 0.3, ν_{rt} = 0.3, G_{lr} = 400 MPa, G_{lt} = 250 MPa, G_{rt} = 25 MPa). The steel material used for the angle bracket was treated as a tri-linear elastic–plastic material with a 0.2% yield stress of 240 MPa, a 1.0% yield stress of 270 MPa, and an ultimate tensile strength of 530 MPa (with strain ϵ = 50%).

It should be remarked that the connection nonlinearity is concentrated in the fasteners and bracket: each nail is represented by a two-degree-of-freedom connector with independent, nonlinear force–slip laws in withdrawal and in-plane transverse directions, calibrated from single-nail tests. These laws intentionally incorporate the local wood–fastener mechanisms (embedment/crushing, hole clearance, nail bending/withdrawal) so that additional plasticity in the CLT shells would double-count the same effects. Post-processing of the FE simulations confirms that, up to peak load, the majority of relative slip across the joint occurs in the connectors

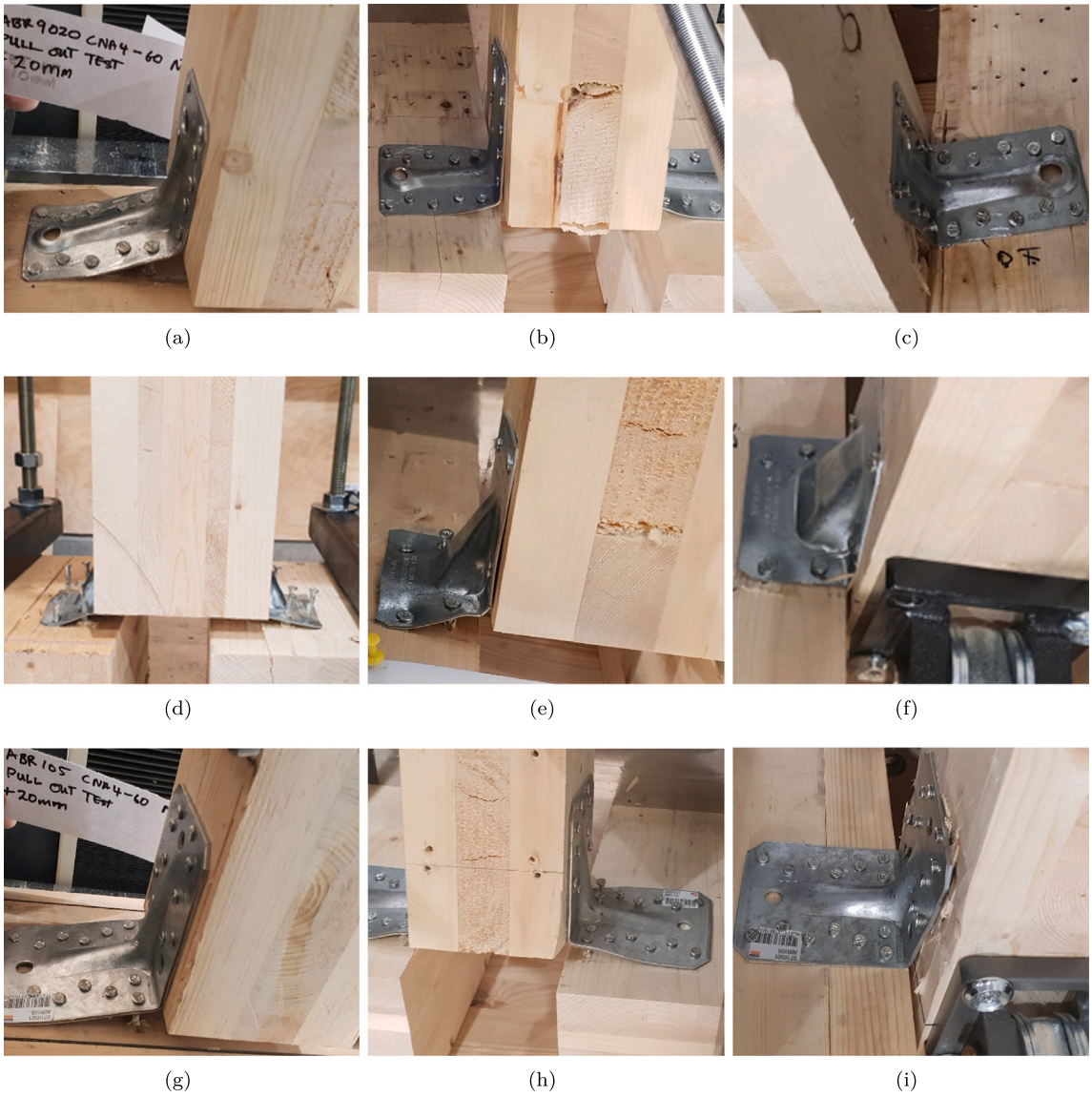

Fig. 7. Failure of the tested specimens (a) ABR9020-U, (b) ABR9020-R, (c) ABR9020-S, (d) HGA105-U, (e) HGA105-R, (f) HGA105-S, (g) ABR105-U, (h) ABR105-R, (i) ABR105-S.

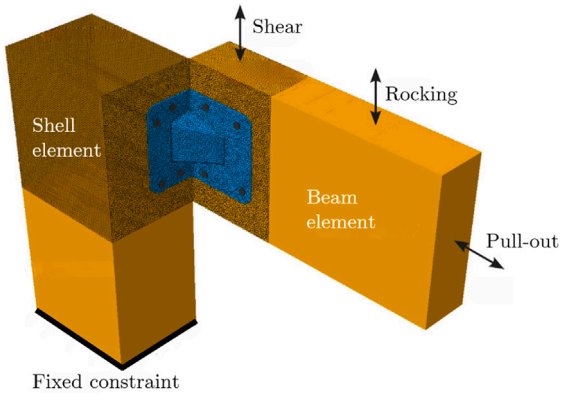

Fig. 8. Detail of the FE model of the connection.

Table 6
Connection finite element model parameters and scatters with respect to experimental values: initial stiffness (k_i), slip modulus (k_s), ultimate force f_u and ultimate displacement u_u of connections. $\%\Delta$ is the relative percentage difference between the FE model output and experimental data.

Configuration	k_i (kN/mm)	$\%\Delta$	k_s (kN/mm)	$\%\Delta$	f_u (kN)	$\%\Delta$	u_u (mm)	$\%\Delta$
ABR9020-U	3,68	−1%	3,62	−2%	16,9	−7%	7,4	−7%
ABR9020-R	0,09	45%	0,09	59%	3,6	4%	80,0	0%
ABR9020-S	1,47	−38%	1,43	−43%	43,4	35%	40,0	66%
HGA10-U	1,57	−9%	1,63	−33%	12,7	−6%	10,1	−31%
HGA10-R	0,09	−34%	0,10	−33%	2,6	−4%	39,0	−27%
HGA10-S	1,03	−15%	1,07	−17%	28,7	45%	36,8	104%
ABR105-U	3,75	1%	3,87	−16%	24,7	−31%	8,3	−14%
ABR105-R	0,17	−18%	0,18	−4%	5,1	−35%	80,0	−3%
ABR105-S	1,95	−13%	1,93	−14%	49,6	51%	40,0	87%

while shell strains in the timber remain within the elastic range of the outer lamellae. Note that brittle perpendicular-to-grain splitting observed in one shear setup is not modelled.

As discussed in the previous section, the brackets, which are significantly different in shape and geometry, exhibit considerable variations in their resistance to load and deformation characteristics.

Fig. 6 displays the overlay of experimental and numerical curves to validate the FE model. Although no formal calibration was performed, there is a notable correspondence between the numerical and experimental curves regarding capacity for all three test configurations, except for ABR105-U, which exhibits a higher actual capacity. However, since only one test repetition was conducted, whether this is an outlier is unclear. Still, the relative difference between the peaks is less than 10%. All curves accurately capture the system's elastic stiffness but fail to describe the post-peak response accurately. While in some cases, such as ABR9020, there is a capability to reproduce the ductile behaviour quite faithfully, in others, it is slightly underestimated. The curves show a brittle behaviour experimentally with sudden capacity degradation for shear tests.

Fig. 9 shows the stress plots of the three angle brackets at failure in the three loading scenarios. In the case of HGA10, the very stiff rib causes a concentration of stress predominantly in the lower wing and around the rib in the upper wing. The ABR series, which includes ABR9020 and ABR105 plotted side by side, is characterized by similarly shaped ribs that lead to a similar stress distribution, with peaks occurring at the bends and on the same rib, unlike in HGA where the rib was relatively unstressed.

Table 6 displays the initial stiffness (k_i), slip modulus (k_s), ultimate force (f_u), and ultimate displacement (u_u) of the FE connections, alongside the percentage difference relative to the experimental value for each parameter.

The trends generally align, and the values fall within an acceptable range. The differences can be attributed to factors such as uncertainties in material properties and the limited number of tests conducted.

It is observed that the Abaqus simulations consistently underestimate the stiffness of the smaller angle bracket, HGA10kt, compared to the larger ABR9020 and ABR105 brackets in all cases (pull-out, shear, and rocking). This might reflect the influence of the group effect described in [62]. A more accurate match between the experimental and Abaqus curves could be achieved by evaluating the effective number of fasteners, regardless of nail spacing, as recommended in [63].

The closer agreement between the numerical and experimental curves in the pull-out cases reveals a high fidelity of the FE model.

Both full-scale experimental testing and the Abaqus simulation revealed significant ductility (i.e., failure controlled by the yielding of nails and the plasticization of the steel plate) in the externally loaded connections studied. This ductile behaviour was also observed in an angle bracket with smaller ribs in [64], supporting using angle brackets as ductile connectors in seismic design.

In shear, the lower experimental capacities are explained by a brittle perpendicular-to-grain splitting that initiated at the loaded edges of the CLT block. This is a consequence of the laboratory geometry—two external blocks clamped to the floor and an internal block connected by two angle brackets with a 3 mm gap to eliminate friction—combined with short clear distances from the bracket toe to the timber edges (about 51.5 mm for ABR9020, 41.0 mm for ABR105, and 39.5 mm for HGA10), which reduced confinement and concentrated tension perpendicular to grain ahead of nail rows. Under these conditions, splitting arrested the load path before the nails reached their lateral capacity, as also visible in the observed failure modes. The FE model, which excludes timber splitting by design, reproduces the stiffness and the response up to the experimental failure point; therefore, in practical applications with code-compliant detailing (larger edge distances, manufacturer-recommended layouts, and common use of transverse reinforcement where needed), the governing failure is expected to occur on the nail or plate side, and the model-predicted capacities are representative. This interpretation is consistent with our setup description (three-block arrangement and 3 mm gap), the measured edge distances, and published tests on CLT angle brackets that report ductile steel/fastener-controlled failures when adequate margins are provided [65]. Particularly evident for HGA10 subjected to in-plane shear, the load transmitted through the vertical web into the base leg creates a moment at the bracket heel. The nail group balances this moment, leading to a marked tension–shear interaction: the nail row upstream of the shear direction carries withdrawal/tension in addition to shear, whereas the downstream row is predominantly in bearing/compression. Consistently, the FE von Mises contours in Fig. 9 (HGA10–S) exhibit (i) a pronounced hotspot at the heel and along the inner edge of the vertical leg and (ii) elevated stresses around the upstream nails; with plasticity, stresses spread to the outer nails, indicating force-flow redistribution.

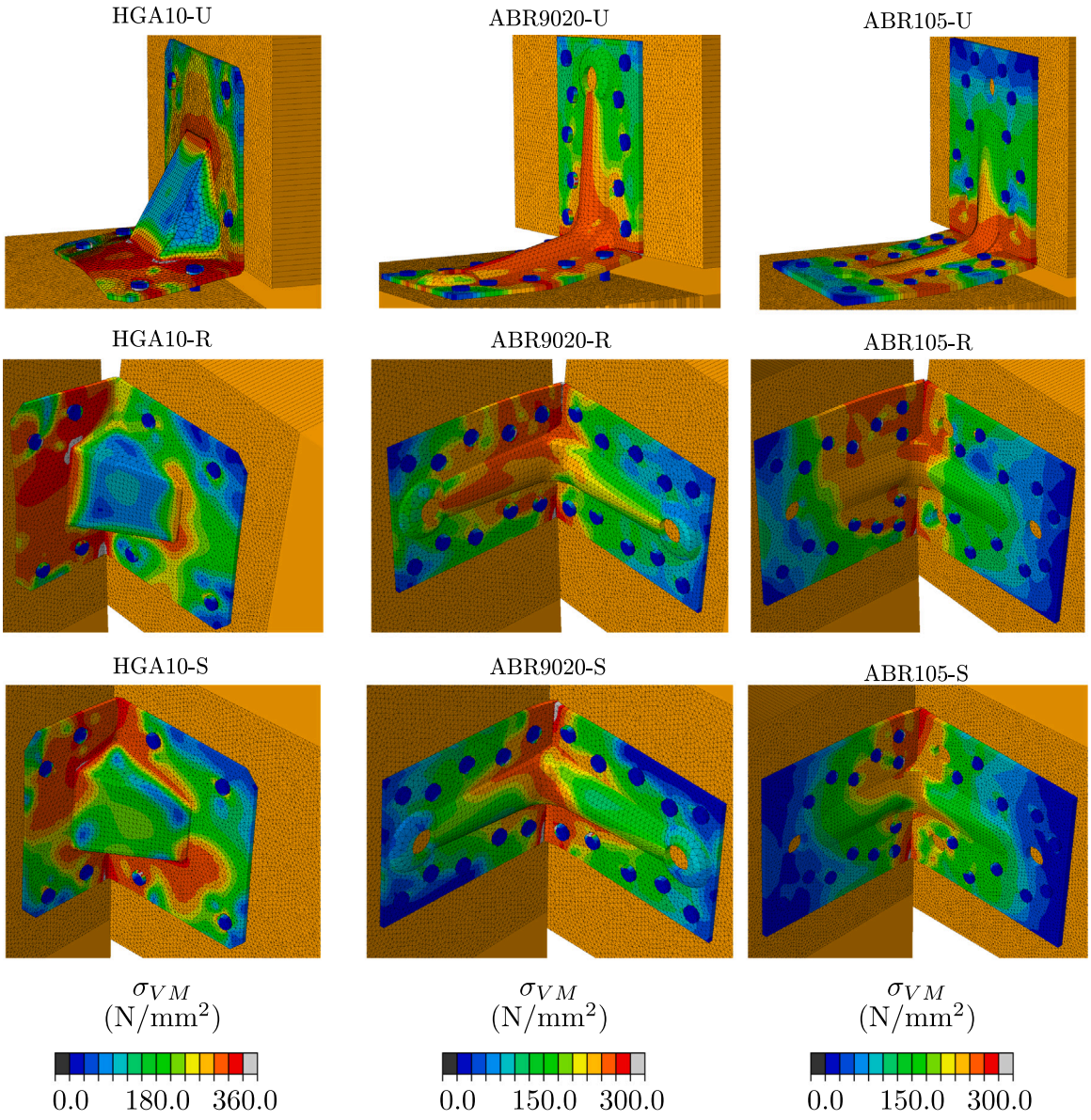

Fig. 9. von Mises stresses according to finite element model at failure.

The CLT panels are modelled as linear–elastic, orthotropic laminated shells; all relevant nonlinearity is confined to the fasteners (two nonlinear force–slip laws per nail, withdrawal and transverse) and to bracket bending. Because the connection deformation is dominated by fastener slip, the global response should be weakly sensitive to the CLT compliance. The authors confirmed this by a parametric check in which the CLT elastic constants (E_L, E_T, G_{LT}, G_{LR}, G_{TR}) were scaled by factors of 5 and 10. Across representative uplift, shear, and rocking cases, the peak capacity was effectively unchanged [<1%], while the initial stiffness varied by at most [<3–5%], with the most significant variation in shear. Hence, the near-rigid-panel limit yields practically the same connection response.

In conclusion, the FE model can be considered sufficiently validated against the experimental data for uncertainty quantification analysis, propagating the uncertainties in the nail-wood interaction through the FE model.

4. Uncertainty quantification analysis and overstrength assessment

This section quantifies how uncertainty in the nail–timber constitutive laws propagates to bracket capacity under withdrawal/uplift, shear, and rocking, and then derives overstrength factors. Fig. 10 outlines the workflow: (1) sample fastener parameters from

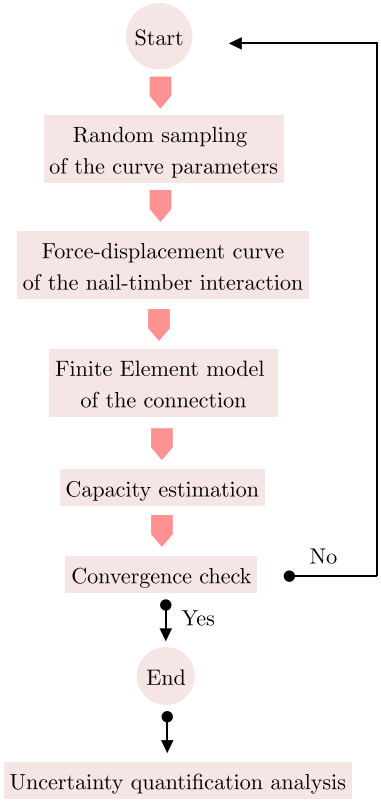

Fig. 10. Flowchart of the main steps of the uncertainty quantification analysis.

Table 7
Definition of the probability density functions assumed for sampling the four physical parameters used to describe the withdrawal (W) and transverse (T) behaviour of the nail-CLT interaction, as per Eq. (1).

Parameter	Label	Direction	Distribution	Mean	CoV
Capacity	f_u [kN]	Withdrawal	Lognormal	2.42	17%
Ultimate displacement	u_u [mm]	Withdrawal	Lognormal	2.68	20%
Secant stiffness	k_r [kN/mm]	Withdrawal	Lognormal	0.06	45%
Residual force at 20 mm	f_r [kN]	Withdrawal	Lognormal	0.52	100%
Capacity	f_u [kN]	Tranversal	Lognormal	4.68	6%
Ultimate displacement	u_u [mm]	Tranversal	Lognormal	17.66	5%
Secant stiffness	k_r [kN/mm]	Tranversal	Lognormal	0.08	29%
Residual force at 20 mm	f_r [kN]	Tranversal	Lognormal	1.30	6%

the probability distributions, (2) generate nail force–slip laws (withdrawal and transverse), (3) run the bracket FE model and extract capacity, and (4) analyse variability and attribution.

4.1. Monte carlo analysis

The authors propagate uncertainty in the eight fastener parameters $\theta = \{f_u, u_u, k_r, f_r\}^{\mathrm{W}} \cup \{f_u, u_u, k_r, f_r\}^{\mathrm{T}}$, using the distributions in Table 7 (means and CoV from single-fastener tests). Unless stated otherwise, they generate $N = 10{,}000$ independent samples. The run is stopped early if the change in CoV of the estimated capacity over the last 500 samples falls below 0.5%; this guards against unnecessary runs while ensuring stable statistics. For each draw of θ, two nail laws (withdrawal/transverse) are instantiated via Eq. (1), applied to the connection model, and the global force–displacement curve is computed.

Table 7 reports the assumed the probability density functions assumed for sampling the four physical parameters used to describe the withdrawal (W) and transverse (T) behaviour of the nail-CLT interaction, as per Eq. (1). The CoV assumed for each parameter originates from the experimental tests on the single fasteners.

The histogram plots of the eight randomly sampled parameters for axial response traverse responses are shown in Fig. 11.

The first 100 generated force–displacement curves of the axial and transverse nail-wood response are shown in Fig. 12. The average curve and the 95% uncertainty bounds, highlighted in light blue, are also shown.

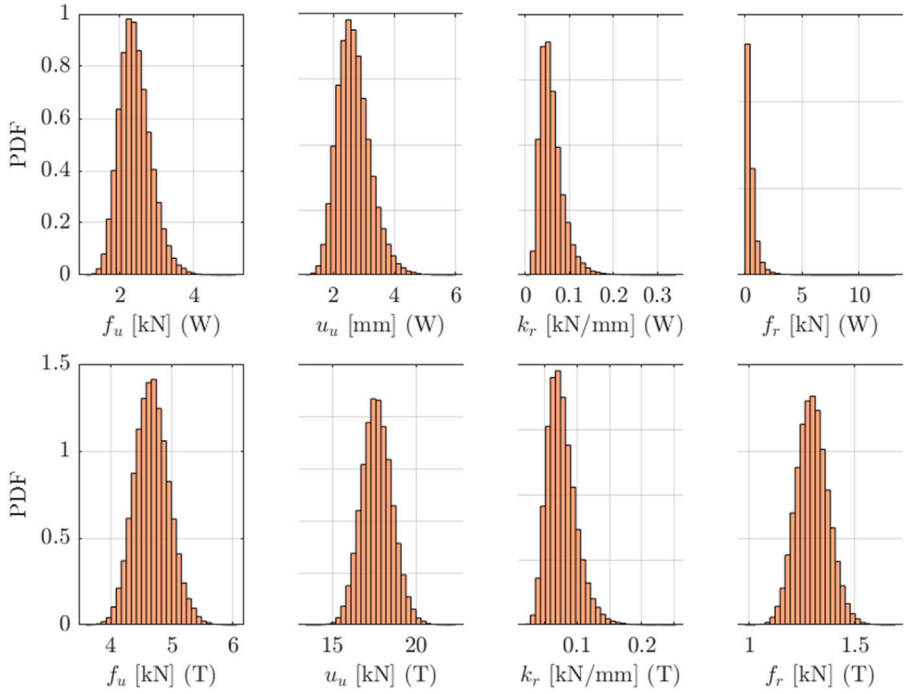

Fig. 11. Histogram plot of the sampled values of the four physical parameters used to describe the withdrawal (W) and transverse (T) behaviour of the nail-CLT interaction, as per Eq. (1).

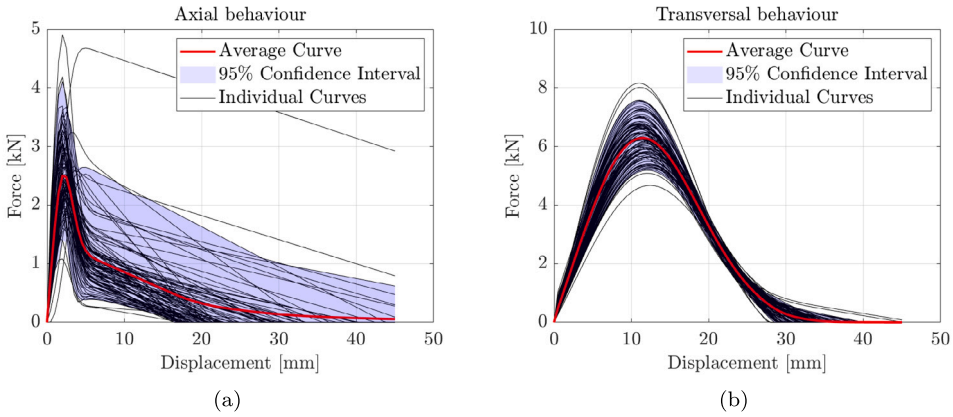

Fig. 12. Overlay of all generated force–displacement curves of the axial and transverse behaviour of the nail-CLT, obtained from the parameters generated by the probability density functions in Table 7. (For interpretation of the references to colour in this figure legend, the reader is referred to the web version of this article.)

Fig. 13 shows an overlay of all the simulated force–displacement curves of the connections, using the nail–timber relationships from Fig. 12 as input. Table 8 presents the statistics of the estimated capacity values in terms of mean and coefficient of variation (CoV).

The analysis of the force–displacement curves shows that the numerical model reaches a maximum capacity but fails to reliably reproduce the post-peak behaviour, with many oscillations after reaching the maximum, indicated by the red cross. For this reason, the authors have reported the curves only up to the maximum value and used them solely for evaluating the capacity value. The main aspects that emerged from the analysis of the results are:

- The variability of capacity values is independent of the types of angle brackets, confirming that it depends more on the modelling of the nail-wood interaction across all models.
- The coefficient of variation of the capacity values is around 18% for pull-out, 13% for rocking, and 4% for shear. This indicates that the parameters defining extraction are characterized by higher variability than those for shear.

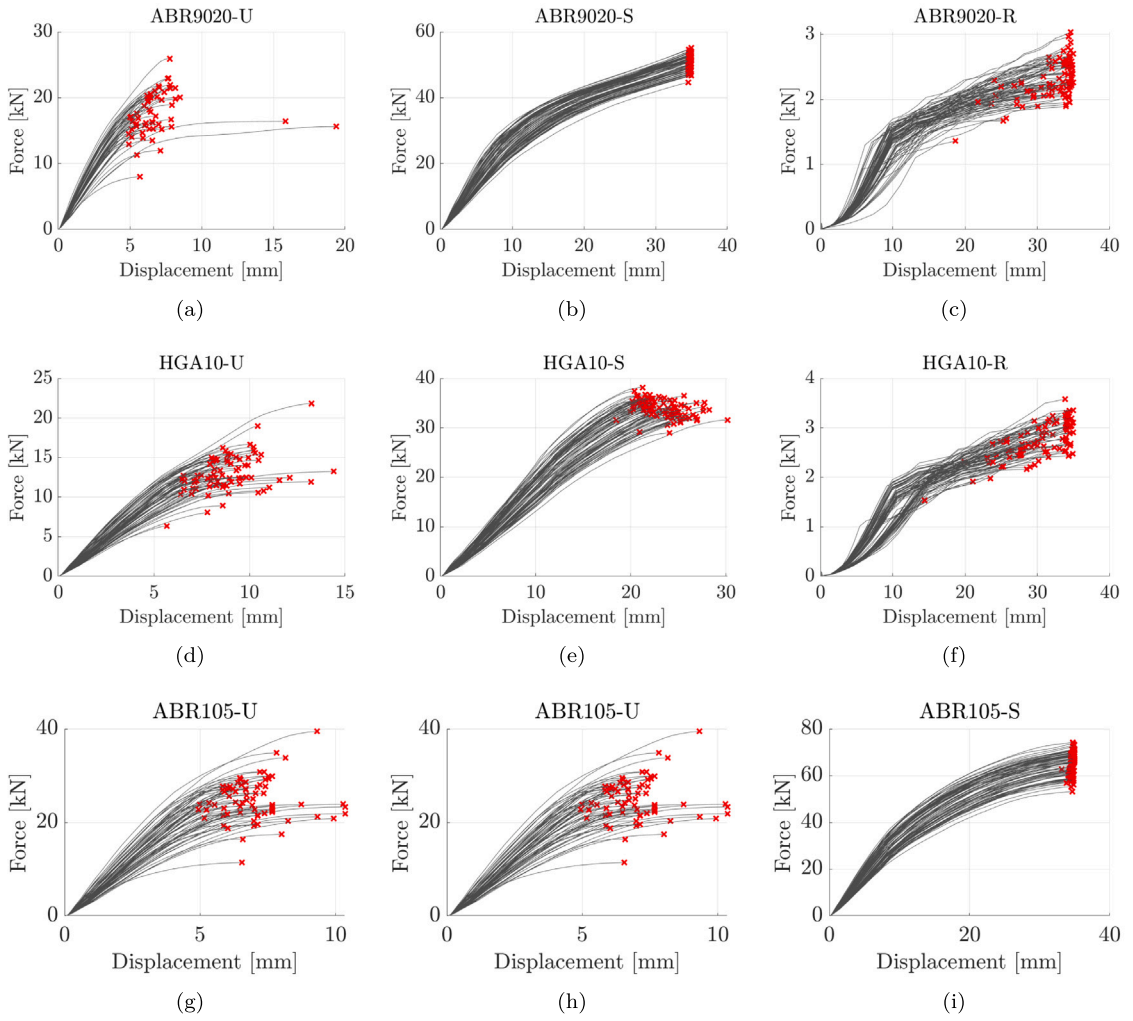

Fig. 13. Overlay of all the simulated force–displacement curves of the connections, using as input the nail–timber relationships in Fig. 12.

Table 8
Mean and coefficient of variation (CoV) of the capacity values of the simulated curves in Fig. 13.

Behaviour	ABR9020		HGA10		ABR105	
	Mean	CoV	Mean	CoV	Mean	CoV
Uplift	17.69	19%	13.09	18%	17.69	19%
Shear	50.61	4%	34.04	5%	50.61	4%
Rocking	2.30	13%	2.74	13%	2.30	13%

- The coefficient of variation for the shear and extraction capacity of the connection roughly coincides with those for nail extraction and shear capacity, at 17% and 6%, respectively.

From this result, it can be inferred that the principal parameter among those defined in Table 7 is the nail's capacity in the two loading directions. However, to understand the role of each parameter in generating the model's response, a model-driven approach was followed in the following paragraph.

In conclusion, the capacity scatter is primarily controlled by the nail–timber laws and is largely independent of bracket type; CoV is about 18% in uplift, 13% in rocking, and 4%–5% in shear, indicating higher intrinsic variability for withdrawal than for transverse response; Additionally the CoV at connection level mirrors the fastener-level CoV for the governing mechanism (withdrawal for uplift/rocking, lateral for shear).

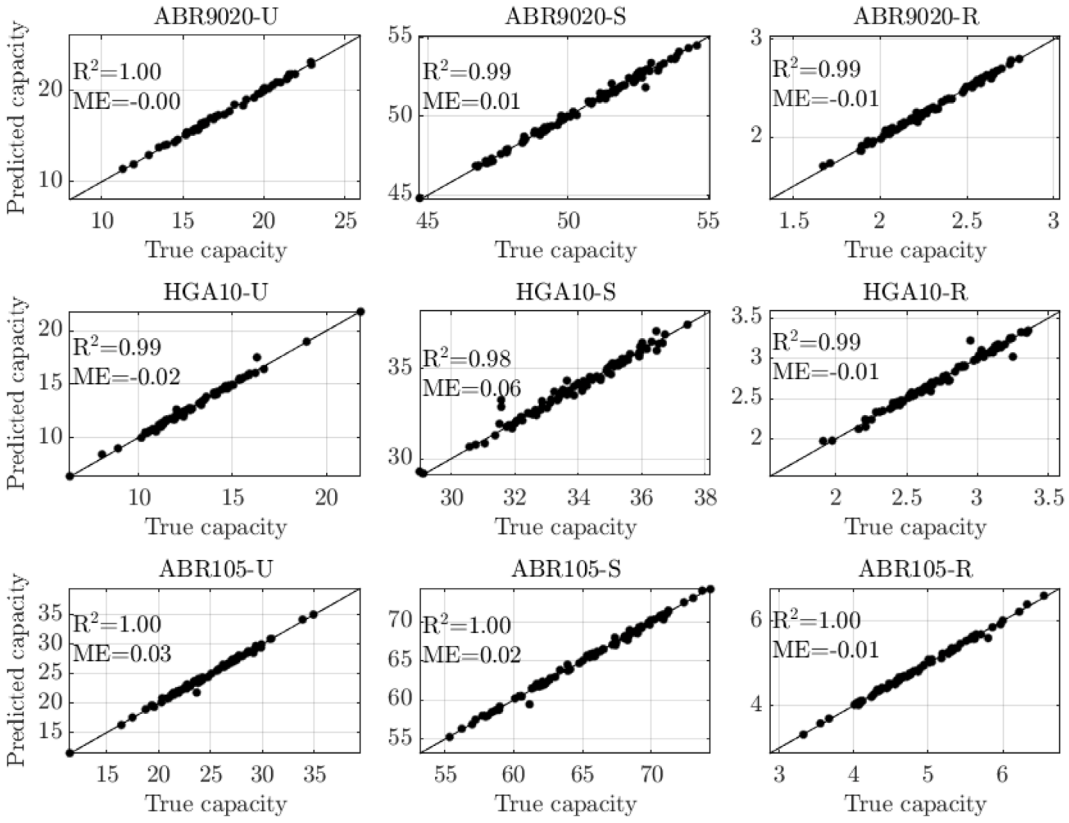

Fig. 14. Predicted vs. true capacity of the nine regression models corresponding to the three angle brackets and loading directions. R^2 and ME indicate the correlation coefficients and the mean error.

4.2. Regression model calibration and variance explanation

To interpret which parameters drive capacity, the authors fit an interpretable surrogate to the FE results for each (bracket, loading) case. They tested several learners and selected a multilinear model with pairwise interactions for its accuracy and transparency. Data are split 80/20 (train/validation) with 5-fold cross-validation on the training set. Fig. 14 shows predicted vs. simulated capacity; R^2 and mean error (ME) are reported in each panel. To compare effect sizes, inputs are standardized (zero mean, unit variance) before fitting; standardized coefficients are listed in Table A.10 (Appendix). In brief, f_u^{W} dominates uplift and rocking, while f_u^{T} dominates shear; interactions are generally negative (capacity-reducing), with a notable quadratic effect of u_u^{W} in rocking.

Fig. 14 shows the predicted vs. FE simulated capacity of the nine regression models corresponding to the three angle brackets and loading directions. R^2 and ME represent the correlation coefficients and the mean error, respectively. Being a surrogate model of a finite element model, the performance metrics are excellent, as expected, and the model can be used as a surrogate to analyse the role of each regressor. For simplicity, R^2 and mean error are reported in each subplot of Fig. 14.

To make the weights of the regressors comparable, the authors estimated the standardized beta coefficients of the regression, obtained by normalizing the explanatory variables and reported in Table A.10 in the Appendix.

The analysis of the regressors with interactions shows that the most influential parameter in determining the extraction capacity is the extraction force of the nail (f_u W). In contrast, for the shear capacity of the bracket, the shear resistance of the nail (f_u T) is the most influential. In rocking, the extraction force is decisive. Regarding the interactions, almost all have a negative coefficient, thus associated with a reduction in capacity, whereas the standardized beta coefficients for the nail capacity are positive. The role of the quadratic interaction of the ultimate displacement at the extraction of the nail in rocking is particularly noteworthy, with a value greater than −0.4. In specific brackets like HGA, the interaction between extraction force and ultimate force also proves significant.

4.3. Variance explanation

This subsection aims to quantify each predictor variable's contribution in explaining the dependent variable's variance derived from finite element models. The analysis is based on the multilinear surrogate models presented in the previous subsection.

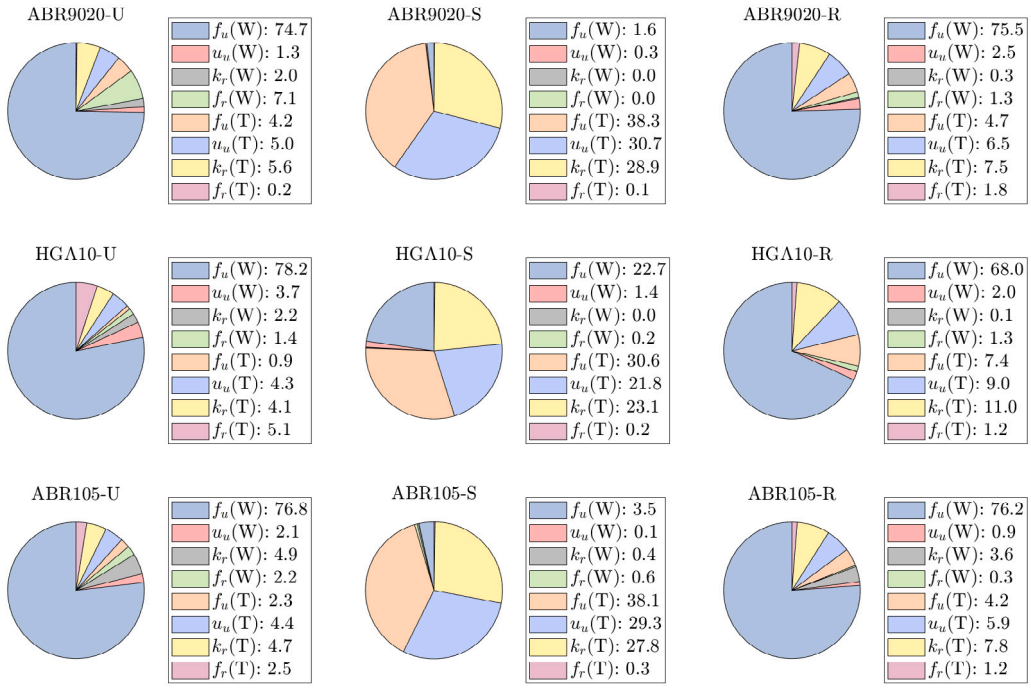

Fig. 15. Pie chart of the percentage explained variance for the nine regression models.

Let **X** represent the matrix of input variables (predictors) and **y** the vector of the output variable (response), the surrogate regression model is defined as

$$\mathbf{y} = \beta_0 + \mathbf{X}\beta + \epsilon \tag{8}$$

where β_0 is the intercept, β represents the coefficients of predictors, and ϵ is the error term. The model is fitted using the least squares method. To determine the explanatory power of each predictor, the total sum of squares (SST) and the sum of squares explained by each predictor is computed:

$$\mathrm{SST} = \sum(\mathbf{y} - \bar{\mathbf{y}})^2 \tag{9}$$

For each predictor j:

$$\mathrm{SS}_j = \mathrm{SST} - \sum(\mathbf{y} - \mathbf{X}_j\beta_j)^2 \tag{10}$$

where $\mathbf{X}_j$ and β_j are the data and coefficients excluding the jth predictor. The percentage of variance explained by each predictor is then calculated as:

$$\mathrm{p}_j = \frac{\mathrm{SS}_j}{\mathrm{SST}} \times 100\% \tag{11}$$

Fig. 15 shows the pie chart of the percentage explained variance for the nine surrogate models.

The analysis of variance can be subdivided based on the loading scenarios:

- **Uplift**: In all three angle brackets, the dominant parameter with the highest p_j is, as expected, $f_u(W)$, the withdrawal capacity of the single nail, accounting for more than 75%. Subsequent parameters play a minor role, generally below 5%, except for the residual force for ABR9010, which reaches 7%. Nevertheless, excluding other parameters, it can be concluded that for uplift, the variance in $f_u(W)$ almost entirely determines the variance in capacity.
- **Shear**: The situation for shear is more complex. In absolute terms, the coefficient of variation of shear capacity is much smaller, oscillating between 4 and 5%. Nonetheless, within this more minor variation, the contributions of various parameters are more nuanced and distinct among the various angle brackets. For ABR9020 and ABR105, the most important parameters, with similar percentage values around 30%, are the three parameters describing the shear response except for the residual force $f_r(T)$. Four parameters are determinant in the more robust angle bracket HGA10 case. In addition to the first three $f_u(T)$, $u_u(T)$, $k_r(T)$, there is also $f_u(W)$. Therefore, in the case of robust brackets, a significant shear-extraction interaction is observed, with the percentage contribution of $f_u(W)$ similar to $f_u(T)$, $u_u(T)$, $k_r(T)$, and about equal to 20%.

- **Rocking**: For the rocking response, the results are quite consistent among the three angle brackets, with the predominant contributor being the nail extraction resistance $f_u(W)$, around 75% for ABR9020 and ABR105, and slightly lower for HGA10 at 65%. This is followed by the determining contributor of the secant stiffness to shear, which, as expected, determines the redistribution of forces among the nails under the action of a bending moment.

4.4. Overstrength factor estimation

The classical definition of overstrength is based on the following limit state function:

$$\underbrace{\gamma_{Rd} R_{\text{dct,an},d}}_{\text{Demand}} - \underbrace{R_{\text{brt}}}_{\text{Capacity}} \leq 0 \tag{12}$$

Here, R_{brt} represents the load-carrying capacity of the non-ductile element, which is described by a suitable probability distribution, and $R_{\text{dct,an},d}$ is the design load-carrying capacity of the ductile element estimated from an analytical capacity model. Despite its theoretical validity, Eq. (12) is challenging to apply in many situations. The main difficulty comes from the relational definition between brittle and ductile responses, which are difficult to quantify directly from experimental tests where specific failure mechanisms are observed. Three separate failure modes, corresponding to three loading scenarios, were considered in this specific case.

Consequently, overstrength factors were calculated according to the straightforward formulation proposed by Fragiacomo and Jorrissen ($\gamma_{\text{Rd,JF}}$) [43] and a more recent one proposed by Aloisio et al. ($\gamma_{\text{Rd,A}}$) [55]. The improvement of $\gamma_{\text{Rd,JF}}$ compared to $\gamma_{\text{Rd,A}}$ are the followings. (i) The overstrength factor is representative of the actual scatter of the connection parameters observed in real-case scenarios. (ii) The numerator only includes the contribution of the aleatoric uncertainty due to an epistemic correction factor (k) calibrated on the experimental tests. (iii) The reliability target (β) is explicit.

Given that no repetitions of the same experimental test were conducted, the dataset generated from Monte Carlo analyses using the FE model was used to calculate $\gamma_{\text{Rd,JF}}$. Conversely, $\gamma_{\text{Rd,A}}$ allows for the use of both experimental data and model predictions and was calculated using both the experimental value of capacity and the variance of the same as estimated by the model.

Resuming, the definition of the partial overstrength factor according to Jorissen A. & Fragiacomo M., 2011 [43], excluding the contribution of the uncertainty factor γ_M is:

$$\gamma^*_{\text{Rd,JF}} = \frac{R_{\text{dct,mod},0.95}}{R_{\text{dct,an},d}} = \frac{R_{\text{dct,mod},0.95}}{R_{\text{dct,exp},0.05}} \cdot \frac{R_{\text{dct,mod},0.05}}{R_{\text{dct,an},k}} = \gamma_{sc} \cdot \gamma_{an} \tag{13}$$

where $R_{\text{dct,mod},0.95}$ and $R_{\text{dct,mod},0.05}$ are respectively the 95th and 5th percentile of the ductile component capacity distribution; $R_{\text{dct,an},k}$ is the characteristic analytical prediction of the ductile element capacity. The coefficient γ_{sc} expresses the scatter of the experimental connection strength properties, indicating the reliability of the connection. The coefficient γ_{an} approximates the analytical formula for evaluating the capacity.

Conversely, the model-driven partial overstrength factor ($\gamma^*_{\text{Rd,A}}$) according to Aloisio et al. [55] specializes to

$$\gamma^*_{\text{Rd,A}} = \frac{R_{\text{dct,exp}} + k \cdot \beta \cdot \sigma_{\text{mod}}(\boldsymbol{x}, \boldsymbol{\Theta})}{R_{\text{dct,an},k}} \tag{14}$$

where $R_{\text{dct,exp}}$ is the capacity of the ductile mechanisms estimated from the experimental test, $\boldsymbol{x}$ are the FE model parameters and $\boldsymbol{\Theta}$ express their related uncertainty; k comes from the assumption that the ratio between the aleatoric and model standard deviation is constant and independent of the value of the model error and assumed to be equal to 1. β is the chosen reliability target, set equal to 1.64, as in Eq. (13). This represents a hybrid formulation, where the variance is given by the FE model and the expected capacity value from the experimental tests.

The estimation of the shear capacity and the withdrawal of the angle bracket is conducted according to Eurocode 5, finding the minimum among the various failure mechanisms, which for the axial direction is the extraction of nails and for the transverse one is the shear of nails.

$$R_{\text{dct,an},k} = \begin{cases} \text{Uplift} \;\; R_{\text{uplift}} = n_w^{k_{ef,w}} f_{uk}(\text{W}), \\ \text{Shear} \;\; R_{\text{shear}} = n_t^{k_{ef,t}} f_{uk}(\text{T}) \end{cases} \tag{15}$$

where n_w and n_t are the number of nails subjected to withdrawal and shear, $k_{ef,w}$ and $k_{ef,t}$ the reduction factors to estimate the effective number of fasteners for withdrawal and shear, respectively, while $f_{uk}(\text{W})$ and $f_{uk}(\text{T})$ are the withdrawal and shear characteristic capacity of the single nail.

The reduction factors should only be calculated for nails oriented parallel to the grain. However, there are no unique grain directions for CLT due to the crossed layers but rather prevailing directions. In the specific case with a three-layer layout, the calculation refers to the outer layers to evaluate the direction of the grain. Specifically, the nail-to-nail distance is approximately $4d$, with d being the nail diameter in the direction perpendicular to the grain. The nail-to-nail distance parallel to the grain is greater than $15d$ for all angle brackets. Therefore, following the recommendation of Eurocode 5 [66], the reduction factors have been assumed to be equal to one.

Before calculating the overstrength factors, the capacity values for the three angle brackets associated with the three failure mechanisms were depicted in Fig. 16 to illustrate the dispersion of results across different angle brackets and loading scenarios. As

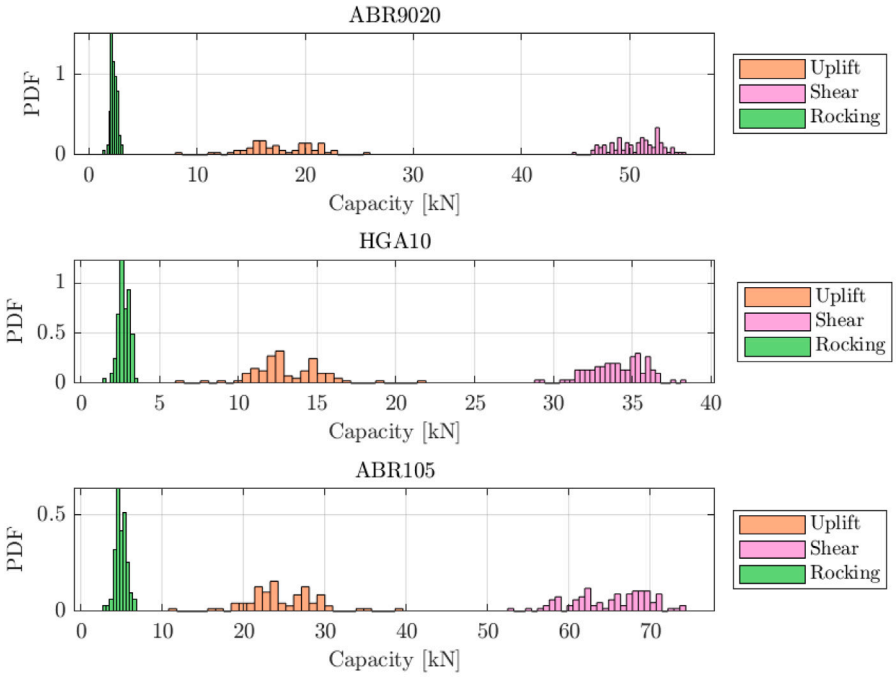

Fig. 16. Histogram plots of the capacity values of the simulated curves in Fig. 13.

Table 9
Overstrength factors according to the formulations in [43] ($\gamma_{Rd,JF}$) and [55] ($\gamma_{Rd,A}$) and intermediate parameters used in the calculation, the characteristic capacity from the analytical model ($R_{dct,an,k}$), the experimental capacity estimate ($R_{dct,exp,}$).

Behaviour	Bracket	FE model			$R_{dct,an,k}$	$R_{dct,exp,}$	$\gamma_{Rd,JF}$	$\gamma_{Rd,A}$
		Mean	CoV	$\sigma_{mod}(\boldsymbol{x},\boldsymbol{\Theta})$				
Uplift	ABR9020	17.69	0.19	3.33	13.86	18.2	1.27	1.71
Shear		50.61	0.04	2.22	42.19	32.2	1.68	/
Uplift	HGA10	13.09	0.18	2.33	6.98	13.5	1.25	2.48
Shear		34.04	0.05	1.79	16.88	19.7	1.88	/
Uplift	ABR105	17.69	0.19	3.33	24.43	36	0.64	1.70
Shear		50.61	0.04	2.22	59.07	33	1.64	/
						Mean Uplift	1.06	2.09
						Mean Shear	1.74	/

previously observed, rocking presents minimal dispersion, whereas uplift and shear show greater variability. The lack of established formulas for calculating rocking capacity, partly because a bending moment on an angle bracket is an unlikely scenario for such a component, has led to the calculation of overstrength factors only for the uplift and shear mechanisms. Moreover, for the shear mechanism, the overstrength factor was calculated solely according to the formulation by Jorissen and Fragiacomo, given that the experimental capacity value cannot be deemed reliable for epistemic correction. This is due to it being associated with wood splitting perpendicular to the grain, which does not occur in the model and is also unlikely in reality since the angle bracket always maintains adequate margins relative to the edges of the element it is anchored to, thus preventing failure due to timber splitting induced by the fasteners.

Table 9 displays overstrength factors according to the formulations in Jorissen and Fragiacomo [43] ($\gamma_{Rd,JF}$) and Aloisio et al. [55] ($\gamma_{Rd,A}$), as well as intermediate parameters used in the calculation, such as the characteristic capacity from the analytical model ($R_{dct,an,k}$), and the experimental capacity estimate ($R_{dct,exp}$).

On average, ($\gamma_{Rd,A}$) is higher than ($\gamma_{Rd,JF}$) due to the use of the experimental capacity value, which, in the case of uplift, is slightly higher than the mean value from the FE model. Furthermore, it is observed that the values of $\gamma_{Rd,JF}$ for shear are slightly higher than those for uplift due to a more significant discrepancy between the analytical and FE capacity values. The average for uplift and shear of $\gamma_{Rd,JF}$ is approximately 1.1 and 1.7, respectively, while for uplift according to $\gamma_{Rd,A}$, which is more conservative, it is about 2.

The overstrength factors are slightly higher than the experimental results obtained in previous testing campaigns. Sustersic [67] estimated the overstrength for nailed hold-downs and angle brackets in CLT panels using Eq. (13), with a γ_{Rd} of approximately 1.3.

Conversely, the obtained values are very similar to those obtained by [68] obtained for nailed angle brackets [7], an overstrength ranging between 1.2 and 1.9.

In recent years, multiple types of angle brackets have been characterized experimentally. However, these testing campaigns addressed other topics, such as the coupling effect on CLT angle brackets [65,69], without tackling the estimation of the overstrength factor. For this reason, there are not many studies that further validate the obtained values of overstrength factors.

5. Conclusions

The study investigates the behaviour of three commercial angle brackets for timber structures produced by Simpson Strong-Tie (ABR9020, ABR105 and HGA10) under three loading conditions: pull-out, shear, and rocking. The rocking load corresponds to a shear force applied at a lever arm of 205 mm to the base wing of the angle bracket. A significant novelty of this research is its focus on the uncertainty in the nail-wood constitutive relationship and how this affects the capacity under each of the three loading scenarios.

The authors developed two models to address this uncertainty. The first, an empirical model, predicts the axial and lateral responses of a single nail based on experimental data included in the study. The second model is a numerical finite element (FE) model that estimates the capacity of the connection with angle brackets in the three loading scenarios. Each nail is represented by two series of equivalent nonlinear springs, defined by the mentioned empirical constitutive relationship. This FE model has been validated by comparing its results against the experimental test of the angle brackets under the three load directions.

Further, a Monte Carlo analysis was performed, assuming variability in the nail-wood bond. This involved randomly generating constitutive relationships for the nail-wood interface based on input simplified parameters determined by suitable probability density functions. The resulting dataset was used to calibrate a surrogate model to predict the load capacity and to explain the variance in responses, attributing it to specific input parameters of the nail-wood bond.

The variance analysis revealed that the main variability in extraction and rocking modes is primarily due to the uncertainty surrounding the nail withdrawal strength. In contrast, the shear response showed greater complexity, with three parameters of the shear constitutive relationship (ultimate strength, slip modulus, and ultimate displacement) playing crucial roles in overall variance. The nail pull-out strength for the HGA10 angle bracket also significantly affects the results, particularly due to a notable interaction between shear and extraction forces in stub elements.

Lastly, overstrength factors were computed following two literature-based formulations. The more conservative approach cited in [55] yielded an overstrength factor of approximately 2.1, whereas, for shear, it was about 1.74 as per [43]. The authors did not calculate the overstrength factor for rocking due to the lack of a reliable analytical method to estimate the capacity in this loading scenario.

In future research, the methodology developed in this paper will be upscaled to complete CLT shear walls by representing each hold-down and base bracket as an equivalent, probabilistic spring with two independent nonlinear laws (withdrawal and in-plane shear) calibrated from the present single-nail/connection evidence. A wall-level macro-model (rigid-body rocking with vertical and shear springs along the base, or a low-order orthotropic panel model with discrete springs at anchor locations) then enforces compatibility and equilibrium, so that uplift forces, base shear and overturning are shared among many connectors according to their stiffnesses.

CRediT authorship contribution statement

Petr Sejkot: Writing – review & editing, Visualization, Validation, Supervision, Software, Resources, Project administration, Methodology, Investigation, Funding acquisition, Formal analysis, Data curation, Conceptualization. **Angelo Aloisio:** Writing – review & editing, Writing – original draft, Visualization, Validation, Supervision, Software, Resources, Methodology, Investigation, Formal analysis, Data curation, Conceptualization. **Yuri De Santis:** Writing – review & editing, Visualization, Validation, Supervision, Software, Methodology, Investigation, Formal analysis, Data curation, Conceptualization. **Massimo Fragiacomo:** Writing – review & editing, Supervision, Conceptualization. **Asif Iqbal:** Writing – review & editing, Visualization, Supervision, Resources, Project administration, Methodology, Funding acquisition, Formal analysis, Data curation, Conceptualization.

Declaration of competing interest

All authors have participated in (a) conception and design, or analysis and interpretation of the data; (b) drafting the article or revising it critically for important intellectual content; and (c) approval of the final version.

This manuscript has not been submitted to, nor is under review at, another journal or other publishing venue.

The authors have no affiliation with any organization with a direct or indirect financial interest in the subject matter discussed in the manuscript

Acknowledgements

This work has been supported by the Ministry of Culture of the Czech Republic, research grant NAKI II DG18P02OVV012 - Sustainable Management of Historical Buildings. It has been partially supported by Forestry Innovation Investment of British Columbia, Canada. The brackets were provided by Simpson Strong-Tie Canada. All supports are gratefully acknowledged. All authors have read and approved the final manuscript.

Table A.10
Standardized beta coefficients of the multi-linear linear regressions.

Norm. Regressor	ABR9020			HGA10			ABR105		
	Standardized beta coefficients								
Intercept	−0.02	0.09	0.11	0.00	0.16	0.14	0.02	0.15	0.03
f_u(W)	0.97	0.09	1.13	1.04	0.62	1.14	1.02	0.17	0.99
u_u(W)	0.07	0.02	0.04	0.09	−0.05	0.10	0.13	0.08	0.05
k_r(W)	0.14	0.01	0.06	0.08	−0.01	0.04	0.07	0.05	0.12
f_r(W)	0.11	−0.01	0.06	0.08	0.07	0.04	0.06	0.11	0.13
f_u(T)	0.06	0.84	−0.02	−0.08	0.61	0.00	0.05	0.79	0.00
u_u(T)	−0.09	−0.13	−0.15	−0.16	0.21	−0.12	−0.04	−0.13	−0.09
k_r(T)	0.09	−0.07	0.05	0.06	−0.30	0.01	0.06	−0.08	0.03
f_r(T)	0.01	−0.04	0.04	0.04	−0.02	0.00	−0.03	0.00	−0.01
f_u(W)-u_u(W)	0.02	0.08	0.14	0.08	0.18	0.43	0.07	0.08	0.04
f_u(W)-k_r(W)	−0.01	−0.08	−0.10	−0.07	−0.19	−0.18	−0.06	−0.03	−0.02
f_u(W)-f_r(W)	−0.01	−0.07	−0.23	−0.09	−0.35	−0.40	−0.09	−0.05	−0.11
f_u(W)-f_u(W)	0.10	0.01	0.15	0.04	−0.05	0.24	0.00	0.04	−0.02
f_u(W)-u_u(T)	0.15	−0.15	−0.08	−0.14	0.19	0.06	−0.12	0.00	−0.11
f_u(W)-k_r(T)	−0.05	0.11	0.15	0.18	−0.14	0.10	0.09	0.04	0.09
f_u(W)-f_r(T)	−0.10	−0.01	−0.08	0.01	−0.01	−0.16	0.01	−0.03	0.01
u_u(W)-k_r(W)	0.01	−0.01	−0.08	0.01	−0.02	−0.08	0.01	−0.06	−0.03
u_u(W)-f_r(W)	0.13	0.00	−0.04	0.00	−0.09	−0.06	0.01	−0.04	−0.04
u_u(W)-f_u(W)	0.20	0.12	−0.20	−0.20	0.04	−0.37	−0.08	−0.15	0.03
u_u(W)-u_u(T)	0.18	−0.16	−0.47	−0.38	0.14	−0.44	−0.14	−0.23	−0.03
u_u(W)-k_r(T)	−0.02	0.17	0.23	0.19	0.12	0.20	0.07	0.07	0.08
u_u(W)-f_r(T)	−0.13	−0.03	0.14	0.18	−0.11	0.19	0.09	0.15	0.03
k_r(W)-f_r(W)	0.05	0.00	−0.02	0.01	0.06	0.01	−0.01	0.04	0.01
k_r(W)-f_u(W)	−0.30	−0.04	0.16	0.17	−0.25	0.19	−0.04	0.03	−0.04
k_r(W)-u_u(T)	−0.26	0.01	0.31	0.35	−0.39	0.21	0.11	0.09	0.00
k_r(W)-k_r(T)	−0.02	−0.04	−0.15	−0.20	0.09	−0.09	−0.14	−0.06	−0.07
k_r(W)-f_r(T)	0.20	0.01	−0.07	−0.15	0.21	−0.08	0.03	−0.04	0.02
f_r(W)-f_u(W)	−0.12	−0.10	0.19	0.11	−0.18	0.30	0.00	0.09	0.01
k_r(W)-u_u(T)	−0.21	−0.03	0.25	0.22	−0.13	0.18	0.18	0.16	0.05
k_r(W)-k_r(T)	0.12	−0.05	−0.05	−0.11	−0.12	−0.01	−0.12	−0.05	−0.07
k_r(W)-f_r(T)	0.11	0.06	−0.10	−0.11	0.15	−0.15	−0.04	−0.11	−0.05
f_u(W)-u_u(T)	−0.06	0.01	0.02	0.03	−0.06	0.02	−0.01	0.05	0.00
f_u(W)-k_r(T)	0.03	0.11	0.04	−0.07	−0.07	0.03	0.08	0.15	−0.07
f_u(W)-f_r(T)	0.03	−0.03	0.00	0.01	−0.07	0.02	−0.02	−0.08	−0.01
u_u(T)-k_r(T)	0.00	0.04	0.10	0.00	−0.15	0.09	0.07	0.11	−0.02
u_u(T)-f_r(T)	0.04	0.04	0.07	0.06	0.10	0.05	−0.02	0.04	−0.01
k_r(T)-f_r(T)	0.01	−0.01	−0.11	−0.05	0.08	−0.07	−0.04	−0.10	0.04

Appendix

See Table A.10.

Data availability

Data will be made available on request.

References

[1] X. Sun, M. He, Z. Li, Novel engineered wood and bamboo composites for structural applications: state-of-art of manufacturing technology and mechanical performance evaluation, Constr. Build. Mater. 249 (2020) 118751.

[2] M. He, X. Sun, Z. Li, W. Feng, Bending, shear, and compressive properties of three- and five-layer cross-laminated timber fabricated with black spruce, J. Wood Sci. 66 (2020) 38.

[3] S. Ukyo, K. Shindo, A. Miyatake, Evaluation of rolling shear modulus and strength of Japanese cedar cross-laminated timber (CLT) laminae, J. Wood Sci. 65 (2019) 31.

[4] Z. Huang, L. Jiang, C. Ni, Z. Chen, The appropriacy of the analytical models for calculating the shear capacity of cross-laminated timber (CLT) under out-of-plane bending, J. Wood Sci. 69 (2023) 14.

[5] N. Mohd Yusof, P. Md Tahir, S. Lee, M. Khan, R. James, Mechanical and physical properties of cross-laminated timber made from Acacia mangium wood as function of adhesive types, J. Wood Sci. 65 (2019) 20.

[6] Y. Bao, W. Lu, K. Yue, H. Zhou, B. Lu, Z. Chen, Structural performance of cross-laminated timber-concrete composite floors with inclined self-tapping screws bearing unidirectional tension–shear loads, J. Build. Eng. 55 (2020) 104653.

[7] I. Gavric, M. Fragiacomo, A. Ceccotti, Cyclic behavior of CLT wall systems: Experimental tests and analytical prediction models, J. Struct. Eng. 141 (11) (2015) 04015034.

[8] I. Gavric, M. Fragiacomo, A. Ceccotti, Cyclic behavior of typical metal connectors for cross-laminated (CLT) structures, Mater. Struct. 48 (6) (2015) 1841–1857.
[9] R. Tomasi, I. Smith, Experimental characterization of monotonic and cyclic loading responses of CLT panel-to-foundation angle bracket connections, J. Mater. Civ. Eng. 27 (6) (2014) 04014189.
[10] M. Izzi, G. Flatscher, M. Fragiacomo, G. Schickhofer, Experimental investigations and design provisions of steel-to-timber joints with annular-ringed shank nails for cross-laminated timber structures, Constr. Build. Mater. 122 (2016) 446–457.
[11] Screws for Use in Timber Construction, ETA-11/0030, European Technical Assessment, ETA, Denmark, 2016.
[12] X. Sun, M. He, Z. Li, F. Lam, Seismic performance of energy-dissipating post-tensioned CLT shear wall structures I: shear wall modeling and design procedure, Soil Dyn. Earthq. Eng. 131 (2020) 106022.
[13] J. Liu, F. Lam, Experimental test of coupling effect on CLT angle bracket connections, Eng. Struct. 171 (2018) 862–873.
[14] J. Liu, F. Lam, Experimental test of coupling effect on CLT hold-down connections, Eng. Struct. 178 (2019) 586–602.
[15] J. Liu, F. Lam, R. Foschi, M. Li, Modeling the coupling effect of CLT connections under biaxial loading, J. Struct. Eng. 146 (4) (2020) 04020040.
[16] L. Pozza, B. Ferracuti, M. Massari, M. Savoia, Axial-shear interaction on CLT hold-down connections—experimental investigation, Eng. Struct. 160 (2018) 95–110.
[17] L. Pozza, A. Saetta, M. Savoia, D. Talledo, Coupled axial-shear numerical model for CLT connections, Constr. Build. Mater. 150 (2017) 568–582.
[18] M. Masroor, G. Doudak, D. Casagrande, The effect of bi-axial behaviour of mechanical anchors on the lateral response of multi-panel CLT shearwalls, Eng. Struct. 224 (2020) 111202.
[19] X. Sun, M. He, Z. Li, An experimental and numerical study on the coupling effect of CLT wall-to-floor angle bracket connections, J. Wood Sci. 69 (1) (2023) 31.
[20] P. Sejkot, A. Aloisio, V. Obradovic, A. Iqbal, Experimental, finite element and analytical characterization of hysteretic response of ductile connections with nailed angle brackets for mass timber structures, Can. J. Civ. Eng. (ja) (2024).
[21] J. Brown, M. Li, A. Palermo, S. Pampanin, F. Sarti, 2021, p. 13, cited By 1.
[22] L.-M. Ottenhaus, M. Li, T. Smith, P. Quenneville, Mode cross-over and ductility of dowelled LVL and CLT connections under monotonic and cyclic loading, J. Struct. Eng. (US) 144 (7) (2018) http://dx.doi.org/10.1061/(ASCE)ST.1943-541X.0002074, cited By 25.
[23] A. Aloisio, F. Boggian, R. Tomasi, M. Fragiacomo, The role of the hold-down in the capacity model of LTF and CLT shear walls based on the experimental lateral response, Constr. Build. Mater. 289 (2021) 123046.
[24] T. Tannert, C. Loss, Contemporary and novel hold-down solutions for mass timber shear walls, Buildings 12 (2) (2022) 1–14, http://dx.doi.org/10.3390/buildings12020202.
[25] N. Chan, A. Hashemi, P. Zarnani, P. Quenneville, Pinching-free connector for timber structures, J. Struct. Eng. (US) 147 (5) (2021) http://dx.doi.org/10.1061/(ASCE)ST.1943-541X.0002982, cited By 7.
[26] A. Aloisio, M. Pelliciari, A.V. Bergami, R. Alaggio, B. Briseghella, M. Fragiacomo, Effect of pinching on structural resilience: Performance of reinforced concrete and timber structures under repeated cycles, Struct. Infrastruct. Eng. 19 (12) (2023) 1728–1744.
[27] A. Aloisio, A. Contento, R. Alaggio, B. Briseghella, M. Fragiacomo, Probabilistic assessment of a light-timber frame shear wall with variable pinching under repeated earthquakes, J. Struct. Eng. 148 (11) (2022) 04022178.
[28] A. Ceccotti, M. Follesa, M. Lauriola, C. Sandhaas, SOFIE project–test results on the lateral resistance of cross-laminated wooden panels, in: Proceedings of the First European Conference on Earthquake Engineering and Seismicity, vol. 3, 2006.
[29] A. Ceccotti, C. Sandhaas, M. Okabe, M. Yasumura, C. Minowa, N. Kawai, SOFIE project–3D shaking table test on a seven-storey full-scale cross-laminated timber building, Earthq. Eng. Struct. Dyn. 42 (13) (2013) 2003–2021.
[30] T. Tannert, C. Loss, Contemporary and novel hold-down solutions for mass timber shear walls, Buildings 12 (2) (2022) 202.
[31] S. Pei, J.W. van de Lindt, A.R. Barbosa, J.W. Berman, E. McDonnell, J. Daniel Dolan, H.-E. Blomgren, R.B. Zimmerman, D. Huang, S. Wichman, Experimental seismic response of a resilient 2-story mass-timber building with post-tensioned rocking walls, J. Struct. Eng. 145 (11) (2019) 04019120.
[32] A. Aloisio, M.M. Rosso, D. Huang, A. Iqbal, M. Fragiacomo, S. Pei, Nonlinear analytical modeling of mass-timber buildings with post-tensioned rocking walls, Bull. Earthq. Eng. 21 (1) (2023) 473–502.
[33] N. Chan, A. Hashemi, S. Agarwal, P. Zarnani, P. Quenneville, Experimental testing of a rocking cross-laminated timber wall with pinching-free connectors, J. Struct. Eng. 149 (10) (2023) 04023132.
[34] A. Polastri, I. Giongo, M. Piazza, An innovative connection system for cross-laminated timber structures, Struct. Eng. Int. 27 (4) (2017) 502–511, http://dx.doi.org/10.2749/222137917X14881937844649, cited By 29.
[35] T. Wright, M. Li, D. Moroder, D. Carradine, 2021, p. 10, cited By 1.
[36] C. Bedon, M. Fragiacomo, Numerical analysis of timber-to-timber joints and composite beams with inclined self-tapping screws, Compos. Struct. 207 (2019) 13–28, http://dx.doi.org/10.1016/j.compstruct.2018.09.008.
[37] M. Izzi, G. Rinaldin, A. Polastri, M. Fragiacomo, A hysteresis model for timber joints with dowel-type fasteners, Eng. Struct. 157 (2018) 170–178.
[38] G. D'Arenzo, G. Rinaldin, M. Fossetti, M. Fragiacomo, An innovative shear–tension angle bracket for cross-laminated timber structures: experimental tests and numerical modeling, Eng. Struct. 197 (2019) 109434.
[39] G. D'Arenzo, D. Casagrande, A. Polastri, M. Fossetti, M. Fragiacomo, W. Seim, CLT shear walls anchored with shear–tension angle brackets: experimental tests and finite-element modeling, J. Struct. Eng. 147 (7) (2021) 04021089.
[40] D. Mitchell, P. Paultre, Ductility and overstrength in seismic design of reinforced concrete structures, Can. J. Civ. Eng. 21 (6) (1994) 1049–1060.
[41] J. Humar, M. Rahgozar, Concept of overstrength in seismic design, in: 11th World Conference on Earthquake Engineering. Acapulco, Mexico, June, vol. 2328, 1996.
[42] D. Trutalli, L. Marchi, R. Scotta, L. Pozza, Capacity design of traditional and innovative ductile connections for earthquake-resistant CLT structures, Bull. Earthq. Eng. 17 (4) (2019) 2115–2136, http://dx.doi.org/10.1007/s10518-018-00536-6, cited By 28.
[43] A. Jorissen, M. Fragiacomo, General notes on ductility in timber structures, Eng. Struct. 33 (11) (2011) 2987–2997, http://dx.doi.org/10.1016/j.engstruct.2011.07.024, cited By 158.
[44] W. Dong, M. Li, L.-M. Ottenhaus, H. Lim, Ductility and overstrength of nailed CLT hold-down connections, Eng. Struct. 215 (2020) http://dx.doi.org/10.1016/j.engstruct.2020.110667, cited By 14.
[45] F. Benedetti, V. Rosales, A. Opazo-Vega, J. Norambuena-Contreras, A. Jara-Cisterna, Experimental and numerical evaluation of hold-down connections on radiata pine cross-laminated-timber shear walls: a case study in Chile, Eur. J. Wood Wood Prod. 77 (1) (2019) 79–92, http://dx.doi.org/10.1007/s00107-018-1365-1, cited By 15.
[46] L.-M. Ottenhaus, M. Li, T. Smith, Structural performance of large-scale dowelled CLT connections under monotonic and cyclic loading, Eng. Struct. 176 (2018) 41–48, http://dx.doi.org/10.1016/j.engstruct.2018.09.002, cited By 23.
[47] L.-M. Ottenhaus, M. Li, T. Smith, P. Quenneville, Overstrength of dowelled clt connections under monotonic and cyclic loading, Bull. Earthq. Eng. 16 (2) (2018) 753–773, http://dx.doi.org/10.1007/s10518-017-0221-8, cited By 27.
[48] X. Zhang, M. Popovski, T. Tannert, High-capacity hold-down for mass-timber buildings, Constr. Build. Mater. 164 (2018) 688–703, http://dx.doi.org/10.1016/j.conbuildmat.2018.01.019, cited By 45.
[49] Z. Chen, Y.-H. Chui, Lateral load-resisting system using mass timber panel for high-rise buildings, Front. Built Environ. 3 (2017) http://dx.doi.org/10.3389/fbuil.2017.00040, cited By 12.

[50] T. Connolly, C. Loss, A. Iqbal, T. Tannert, Feasibility study of mass-timber cores for the UBC tall wood building, Buildings 8 (8) (2018) http://dx.doi.org/10.3390/buildings8080098, cited By 40.
[51] J.W. van de Lindt, M.O. Amini, D. Rammer, P. Line, S. Pei, M. Popovski, Seismic performance factors for cross-laminated timber shear wall systems in the United States, J. Struct. Eng. 146 (9) (2020) 04020172.
[52] M. Schick, T. Vogt, W. Seim, Connections and anchoring for wall and slab elements in seismic design, CIB Work. Comm. W18-Timber Struct. Vanc. Can. (2013).
[53] A. Aloisio, M. Fragiacomo, Reliability-based overstrength factors of cross-laminated timber shear walls for seismic design, Eng. Struct. 228 (2021) 111547.
[54] Y. De Santis, A. Aloisio, D.P. Pasca, I. Gavrić, M. Fragiacomo, Mechanical characterization of soundproofed inclined screws connections, Constr. Build. Mater. 412 (2024) 134641.
[55] A. Aloisio, Y. De Santis, D.P. Pasca, M. Fragiacomo, R. Tomasi, Aleatoric and epistemic uncertainty in the overstrength of CLT-to-CLT screwed connections, Eng. Struct. 304 (2024) 117575.
[56] Simpson Strong-Tie, Connector nail - CNA, 2024, https://www.strongtie.co.uk/en-UK/products/connector-nail-cna.
[57] Y. De Santis, A. Aloisio, D.P. Pasca, I. Gavrić, M. Fragiacomo, Mechanical characterization of soundproofed inclined screws connections, Constr. Build. Mater. 412 (2024) 134641, http://dx.doi.org/10.1016/j.conbuildmat.2023.134641, URL https://www.sciencedirect.com/science/article/pii/S095006182304360X.
[58] R. Foschi, Load-slip characteristic of nails, Wood Sci. (7) (1974).
[59] R.M. Richard, B.J. Abbott, Versatile elastic-plastic stress-strain formula, J. Eng. Mech. Div. 101 (4) (1975) 511–515.
[60] EN 12512:2001 + A1:2005, Timber structures - test methods - cyclic testing of joints made with mechanical fasteners, 2005, 3 (1).
[61] EN-26891, Timber structures - joints made with mechanical fasteners - general principles for the determination of strength and deformation characteristics, 1991,
[62] H. Krawinkler, F. Parisi, L. Ibarra, A. Ayoub, R. Medina, Development of a testing protocol for wood frame structures, CUREE Publ. No. W-02 (2001).
[63] Simpson Strong-Tie, Product catalogue, 2019.
[64] A. Iqbal, P. Sejkot, Finite-element modelling of ductile wood connections, in: Proceedings of Annual Conference of Canadian Society for Civil Engineering, 2019.
[65] J. Liu, F. Lam, Experimental test of coupling effect on CLT angle bracket connections, Eng. Struct. 171 (2018) 862–873.
[66] EN-12512, Timber structures - test methods - cyclic testing of joints made with mechanical fasteners, BSI (2001).
[67] I. Sustersic, B. Dujic, M. Fragiacomo, Influence of the connection modelling on the seismic behaviour of crosslam timber buildings, in: Materials and Joints in Timber Structures: Recent Developments of Technology, Springer, 2014, pp. 677–687.
[68] I. Gavric, M. Fragiacomo, A. Ceccotti, Strength and deformation characteristics of typical X-lam connections, in: World Conference on Timber Engineering, 2012, pp. 146–155.
[69] J. Chen, Z. Peng, T. Furuta, H. Xiong, Mechanical properties and analytical model of a novel dissipative angle bracket for CLT structures, Eng. Struct. 300 (2024) 117229.